Title: Retrograde mitochondrial transport regulates mitochondrial biogenesis in zebrafish neurons

Authors: Angelica E Lang[1, 2], Chris Stein[1], and Catherine M Drerup[1, 2,*]

Affiliations:

[1] Department of Integrative Biology; University of Wisconsin-Madison; Madison, WI 53706

[2] Genetics training program; University of Wisconsin-Madison; Madison, WI 53706

*Corresponding author. Email: drerup@wisc.edu

Abstract: To maintain a healthy mitochondrial population in a long-lived cell like a neuron, mitochondria must be continuously replenished through the process of mitochondrial biogenesis. Because the majority of mitochondrial proteins are nuclear encoded, mitochondrial biogenesis requires nuclear sensing of mitochondrial population health and function. This can be a challenge in a large, compartmentalized cell like a neuron in which a large portion of the mitochondrial population is in neuronal compartments far from the nucleus. Using in vivo assessments of mitochondrial biogenesis in zebrafish neurons, we determined that mitochondrial transport between distal axonal compartments and the cell body is required for sustained mitochondrial biogenesis. Estrogen-related receptor transcriptional activation links transport with mitochondrial gene expression. Together, our data support a role for retrograde feedback between axonal mitochondria and the nucleus for regulation of mitochondrial biogenesis in neurons.

Introduction

Mitochondria are critical for neuronal function and survival. These organelles have many essential roles, including production of ATP, calcium buffering, and the production of metabolites that can function as signaling molecules [1]. For a neuron to maintain a healthy mitochondrial population, mitochondria must be replenished through the process of mitochondrial biogenesis [2]. In other cell types, such as myocytes and adipocytes, indicators of mitochondrial health and function like AMP/ATP and NAD+/NADH ratios as well as calcium signaling stimulate the transcriptional control of mitochondrial biogenesis in the nucleus [3-6]. These upstream signals can activate transcriptional regulators like the PGC-1 (Peroxisome Proliferator-activated Receptor Gamma Coactivator 1) family of transcriptional coactivators [7]. PGC-1α, considered the master regulator of mitochondrial biogenesis, can be activated by phosphorylation or de-acetylation by AMP-activated protein kinase (AMPK) or Sirtuin 1 (SIRT1) respectively [3,4,6]. AMPK activity is stimulated by increases in the AMP/ATP ratio while SIRT1 activity depends on local NAD+ levels. Once activated, PGC-1α can induce the expression of nuclear-encoded mitochondrial proteins through the activation of transcription factors like the nuclear respiratory factors (NRF1/2) or the estrogen related receptors (ERRα/β/γ) [7-10]. How neurons, with mitochondrial populations spread throughout dendritic and axonal arbors, oftentimes large distances from the nucleus, sense mitochondrial health and function to activate these transcriptional pathways is an open and critical question [2].

Mitochondrial biogenesis requires the division and expansion of existing organelles to increase mitochondrial mass. This requires the coordination of several cellular processes. Mitochondrial DNA (mtDNA) must be replicated and the mtDNA nucleoids segregated, after which mitochondrial fission occurs at or near the middle of the organelle [11,12]. Daughter mitochondria are expanded through transcription, translation, and mitochondrial import of nuclear encoded gene products as well as cellular and mitochondrial derived lipids [2,13]. Along with nuclear transcription, mitochondria also synthesize thirteen proteins encoded by mtDNA in the mitochondrial matrix. Given the dependence on coordinated mitochondrial and nuclear gene expression, it is unsurprising that a substantial amount of mitochondrial biogenesis occurs in the perinuclear region in non-neuronal cells [14,15]. In neurons, evidence of mitochondrial biogenesis, including mtDNA replication and synthesis of mitochondrial proteins, has been observed in both the neuronal cell body and in axons of chick, rat, and drosophila [13,16-19]. Mitochondria produced in the neuronal cell body are distributed throughout the expanse of the cell by microtubule-based transport. In neuronal axons, kinesin motor proteins are responsible for axon terminal directed (anterograde) mitochondrial transport while the Cytoplasmic dynein motor transports mitochondria from the periphery back to the cell body (retrograde) [20-23]. A complement of proteins including Trak1/2 and Miro1/2 have been shown to scaffold mitochondria to these motors for transport [24-30]. Disrupting mitochondrial transport into the axon impairs axon development and regeneration after injury [31-33]. Inhibition of retrograde mitochondrial transport from neurites back to the cell body causes mitochondrial accumulation in axonal and dendritic processes and impaired mitochondrial health at the synapse [34-36]. However, the role of retrograde mitochondrial transport in mitochondrial population maintenance in neurons remained undefined.

We hypothesized that transport of mitochondria from distal regions of the neuron to the cell body could link mitochondrial population surveillance and regulation of mitochondrial biogenesis frequency in neurons. Using zebrafish neurons, we show that reducing mitochondrial retrograde

transport from the axon terminal back to the cell body reduces markers of mitochondrial biogenesis, including mtDNA replication, nuclear transcription of mitochondrial genes, and the production of mitochondrial biomass in the cell body. Analysis of mitochondrial turnover at the synapse revealed that reduced mitochondrial biogenesis correlates with reductions in cell body-derived mitochondrial material transported to the axon terminal. Widespread disruption to mitochondrial gene expression in neurons lacking mitochondrial retrograde transport suggests transport plays an important role in regulation of transcriptional programs necessary for mitochondrial biogenesis. We present evidence that this crosstalk is mediated by SIRT1-dependent Estrogen related receptor (ERR) transcriptional activity. Together, our work supports a model in which the retrograde transport of mitochondria is a powerful signaling mechanism to regulate mitochondrial biogenesis in neurons.

Results

Inhibiting mitochondrial retrograde transport disrupts markers of mitochondrial biogenesis in neuronal cell bodies

We used larval zebrafish posterior lateral line (pLL) sensory neurons to study the dynamics of mitochondrial biogenesis in vivo. The pLL system is composed of afferent neurons and sensory organs called neuromasts situated along the trunk [37]. The cell bodies of pLL neurons are clustered in a ganglion (pLLg) near the head while the afferent axons extend down the body and branch into axon terminals that innervate neuromasts (Figure 1A). Axon extension and synapse formation occurs by 4 days post fertilization (dpf; [38]), allowing us to use this system to study mitochondrial populations in a fully formed neuronal circuit in the translucent zebrafish larva. To disrupt retrograde mitochondrial transport in pLL neurons, we used an existing mutant line with a unique loss of function mutation in the gene encoding Actr10 (*actr10*^{nl15}; hereafter referred to as *actr10;* [34,36]). Actr10 is a component of the Cytoplasmic dynein accessory complex dynactin. Complete loss of Actr10 function results in failed cell division, likely due to loss of all dynein motor function [39]. In contrast, the *actr10*^{nl15} mutation in zebrafish causes loss of mitochondrial interaction with the dynein motor, leading to loss of retrograde (cell body directed) mitochondrial transport and accumulation of mitochondria in axon terminals ([34]; Figures 1B and C). This disruption is specific to mitochondria, as other retrogradely moving cargos, including late endosomes, lysosomes, and signaling molecules, are transported normally. Additionally, transmission electron microscopy (TEM) analysis showed accumulations of only mitochondria in axon terminals [34]. Intriguingly, in addition to mitochondrial accumulation in the distal axons, we found a severe reduction in mitochondrial density in the cell body of *actr10* neurons (Figures 1B and C). We asked if this loss of mitochondrial density could be due to loss of mitochondrial biogenesis in *actr10* mutants.

We first analyzed a critical step during biogenesis, mtDNA replication, using immunolabeling for single stranded binding protein 1 (SSBP), which transiently associates with mtDNA to facilitate replication [40]. The number of SSBP puncta was significantly reduced in *actr10* pLL cell body mitochondria (Figures 1D and F). This phenotype is not due to loss of mtDNA as the density of nucleoids labelled with the mtDNA nucleoid protein TFAM (transcription factor A, mitochondria; [41]) is not decreased in *actr10* mutants (Figures 1E and G) and mtDNA nucleoid size was similar between wild type and *actr10* mutants (Figure S1E). SSBP and TFAM antibody efficacy was validated by western (Figure S1F). Together, this data demonstrates a loss of active mtDNA replication in *actr10* mitochondria, suggesting decreased mitochondrial biogenesis.

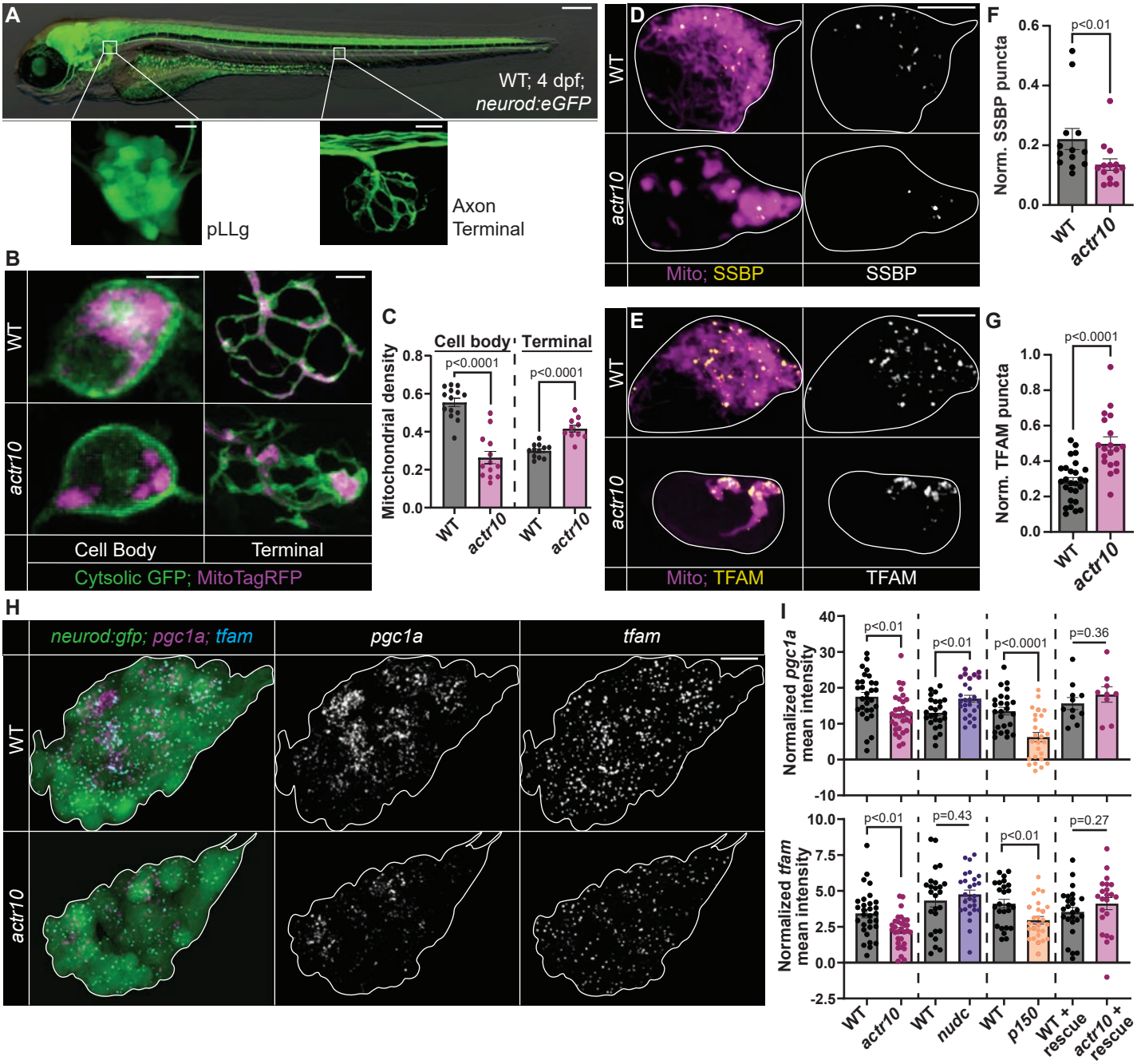

Figure 1: Mitochondrial cell body density and biogenesis markers are reduced in *actr10* mutants. (A) 4 dpf zebrafish transgenic larva carrying the *TgBAC(neurod:egfp)*^{nl1} transgene which labels neurons with GFP. The posterior lateral line gangion (pLLg) and a pLL axon terminal are boxed and magnified. (B) 4 dpf pLLg cell body and pLL axon terminal expressing cytosolic GFP and mitochondria-localized TagRFP (MitoTagRFP, magenta) in wild type and *actr10* mutants. (C) Quantification of mitochondrial density (mitochondrial area/cytosolic area; ANOVAs). (D,E) SSBP and TFAM immunostaining in pLL cell body mitochondria, visualized with mitochondria-localized GFP (Mito, magenta). (F,G) Number of SSBP or TFAM puncta normalized to mitochondrial volume (Wilcoxon). (H) HCR RNA FISH labeling of *pgc1a* and *tfam* mRNA in the pLLg of wild type and *actr10* mutants carrying the *TgBAC(neurod:egfp)*^{nl1} transgene (white outline). (I) pLLg mean fluorescence intensity of *pgc1a* and *tfam* normalized to background (ANOVAs) in wild type, *actr10*, *nudc*, *p150*, and wild type/*actr10* larvae expressing Actr10 in neurons (+ rescue). Scale bars: (A) full larva = 200 µm, insets = 10 µm; (B, D, & E) = 5 µm; (H) = 10 µm. All data are mean ± SEM and points represent individual larvae.

Mitochondrial biogenesis requires coordinated transcription of nuclear encoded mitochondrial genes. This is largely controlled by the PGC-1 family of transcriptional coactivators and their associated transcription factors, including NRF-1/2. Downstream of this transcriptional activation is a plethora of nuclear-encoded mitochondrial genes, including *tfam* [7,10]. We first assessed the expression of *pgc1a*, *pgc1b*, *nrf1*, and *tfam* using colorimetric in situ hybridization and found that all were noticeably reduced in *actr10* mutants (Figures S1A and B). To quantify gene expression of biogenesis markers in the pLLg, we turned to hybridization chain reaction RNA fluorescence in situ hybridization (HCR RNA FISH; [42]). We assessed *pgc1a* and *tfam* expression and confirmed both were significantly reduced in *actr10* mutants (Figures 1H and I). Neuronal rescue of Actr10 in a stable transgenic line (*Tg(5kbneurod:mRFP-actr10)*^{nl22}; [34]) rescued neuronal mitochondrial density (Figures S1C and D) as well as *pgc1a* and *tfam* expression (Figure 1I) confirming loss of Actr10 in neurons underlies this phenotype. To determine if the changes to gene expression in *actr10* mutants could be explained by general disruptions to retrograde cargo transport, we quantified gene expression in control mutant strains with loss of function mutations in *p150a/b* (duplicated gene in teleost fish requiring double knockout) and *nudc* [34,43]. p150 is a component of the dynactin complex that, when mutated, disrupts all retrograde cargo transport, including mitochondria [34,44-46]. NudC is a dynein regulator that, when mutated in zebrafish neurons, disrupts the retrograde transport of late endosomes and autophagosomes without altering the localization or transport of mitochondria [43]. *pgc1a* and *tfam* expression were reduced in *p150* mutants but unaffected in *nudc* mutants, further suggesting the decreased expression of these mitochondrial biogenesis markers was due to the loss of retrograde mitochondrial transport (Figure 1I).

Nuclear transcription of mitochondrial genes is disrupted in actr10 mutant neurons

Given the changes to mtDNA replication and transcription of mitochondrial biogenesis related genes, we decided to look more broadly at how nuclear gene expression of mitochondrial proteins may be altered in *actr10* mutants. We isolated pLL neurons using fluorescence activated cell sorting (FACS) from a novel transgenic line (*Tg(hsp70:eGFP-SILL)*^{unwd12Tg}) and used bulk RNA-sequencing to analyze the transcriptomes of wild type and *actr10* mutant neurons (Figure 2A). Differential gene expression analysis and cross comparisons to the MitoCarta database confirmed that mitochondrial genes are significantly downregulated in *actr10* mutants compared to wild type siblings (Figures 2B and C; [47]). In contrast, there were only 3 mitochondrial genes significantly upregulated (p=0.999, Fisher's exact test). Gene Set Enrichment Analysis of Gene Ontology terms identified Mitochondrial Protein Complexes to be the most significantly de-enriched term in the dataset (Figure 2D; Figure S2A) and KEGG pathway enrichment analysis showed strong enrichment for mitochondrial pathways in downregulated genes (Figure S2B). To confirm our RNA-seq results, we used HCR RNA FISH to quantify pLL ganglion expression of ten downregulated genes and two genes that were not altered in our dataset. These analyses aligned with our RNA-seq data, confirming loss of these mitochondrial transcripts in *actr10* mutants (Figures 2E-H). Additionally, we confirmed these results using colorimetric in situ hybridization of a subset of these genes, showing reduced expression of *atp5md* and *cox5ab* but not the controls *polb* and *tomm40* (Figures S2C and D). Finally, to assess the specificity of the transcriptomic changes, we included positive and negative control mutant strains *p150* and *nudc* described above [34,43]. As predicted, *p150* but not *nudc* mutants have a loss of *cox5ab* expression (Figures 2E and F). Together, this transcriptomic analysis suggests that mitochondrial retrograde transport modulates expression of mitochondrial genes.

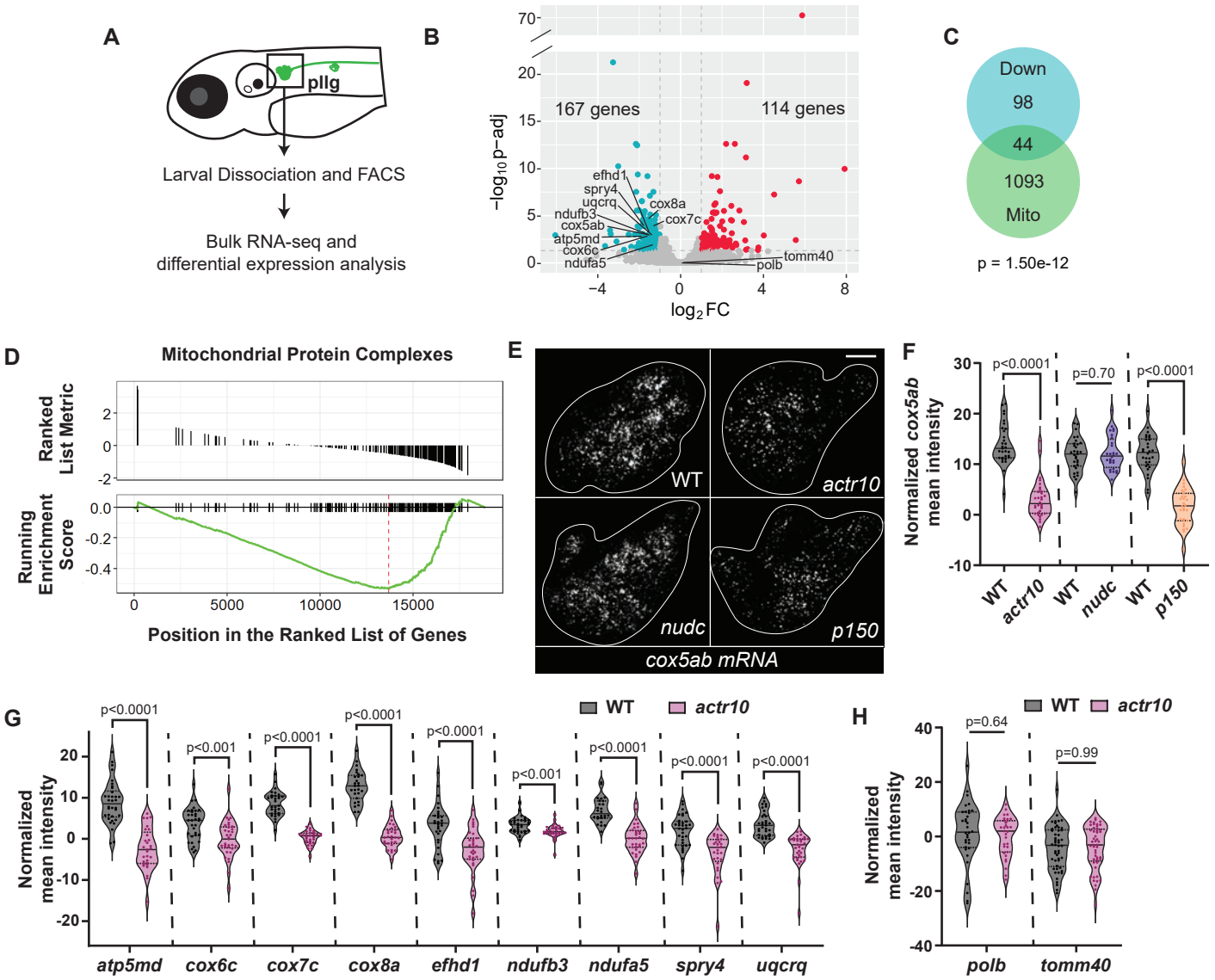

Figure 2: Mitochondrial gene expression is downregulated in *actr10* mutants. (A) RNA-sequencing strategy. (B) Volcano plot showing differential gene expression between wild type and *actr10* mutants. The plot shows -log10(adjusted p-value) vs. log2(Fold Change). Blue dots represent genes significantly downregulated while red dots represent genes significantly upregulated in *actr10* mutants. Genes selected for secondary analysis using HCR RNA FISH are labeled. (C) Overlap between downregulated genes and the MitoCarta3.0 database of the mitochondrial proteome (Fisher's exact test). Human homologs of downregulated zebrafish genes were used for analysis. Duplicated zebrafish paralogues were only counted once. (D) GSEA plot for Mitochondrial Protein Complexes, the most significantly de-enriched gene ontology term in *actr10* mutants relative to wild type. (E) Representative images of HCR RNA FISH labeling of *cox5ab* mRNA in the pLLg (outlined in white) for wild type, *actr10*, *nudc*, and *p150* mutants. Scale bar = 10 µm. (F) pLLg mean fluorescence intensity of *cox5ab* normalized to background (ANOVAs). (G) pLLg mean fluorescence intensity normalized to background for downregulated mitochondrial genes in wild type vs. *actr10* mutants (ANOVAs). (H) pLLg mean fluorescence intensity normalized to background for control genes in wild type vs. *actr10* mutants (ANOVAs). (F-H) Data plot lines represent the median and quartiles; data points represent individual larvae.

Impaired mitochondrial biogenesis decreases the contribution of cell body-derived mitochondria to the axon terminal

In neurons, mitochondria produced by biogenesis in the cell body are transported in the anterograde direction to support the population of mitochondria in the axon terminal [2]. We asked if the contribution of new mitochondrial biomass from the cell body to the axon terminal was disrupted in *actr10* mutants. To do this, we used photo-labeling strategies to first assess the rate of cell body-derived mitochondrial addition to the axon terminal in wild type animals. We expressed photoactivatable GFP (PA-GFP) localized to the mitochondrial matrix in pLL neurons and locally activated the GFP only in the cell body. Then, we quantified the addition of cell body derived mitochondria to the axon terminal at multiple time-points after photo-activation. We found that by 4 to 8 hours post-activation (hpa), ~50% of the mitochondrial density in the axon terminal was cell body-derived (Figures S3A-D). Next, we asked if the amount of cell body-derived mitochondrial material transported to the axon terminal correlated with turnover of the axon terminal mitochondrial population. Published data has shown that axon terminal mitochondria are consistently lost over a period of hours in pLL axon terminals [36]. Using precise activation of matrix-localized PA-GFP in axon terminal mitochondria followed by post-activation imaging, we determined that ~50% of the labeled mitochondrial density is absent from the axon terminal by 8 hpa (Figures S3E-G). This complements the estimated rate of mitochondrial entrance into the axon terminal from the cell body and suggests that cell body-derived mitochondria may play a significant role in maintenance of the axon terminal mitochondrial population.

Given the role for cell body-derived mitochondria in axon terminal turnover, we predicted that decreased biogenesis in the cell body would result in a progressive loss of mitochondrial addition to the axon terminal. To test this, we assessed changes to mitochondrial biogenesis and transport in *actr10* mutants across multiple timepoints post-axon extension: 2, 3, and 4 dpf. Assessment of mitochondrial density in axon terminals and cell bodies of *actr10* mutants demonstrated that mitochondrial density was elevated in axon terminals as early as 2 dpf (Figures S4A and B) and cell body mitochondrial density was notably depleted by 3 dpf (Figures S4C and D). Quantification of the biogenesis markers *pgc1a* and *tfam* using HCR RNA FISH demonstrated that loss of cell body mitochondrial density at 3 dpf corresponded with loss of *pgc1a* expression, followed by loss of *tfam* expression by 4 dpf (Figures 1H and I; Figures S4E and F). This time course confirms that loss of cell body mitochondrial density correlates with decreased markers of mitochondrial biogenesis.

We predicted that the progressive loss of cell body mitochondrial biogenesis in *actr10* mutants would result in reduced anterograde mitochondrial transport. Live imaging of mitochondrial movement in pLL axons demonstrated that retrograde transport was disrupted at 3 dpf while anterograde transport frequency was not altered until 4 dpf (Figures S4G and H; Movies S1-S4). This time series demonstrated retrograde mitochondrial transport is lost first in *actr10* mutants, leading to mitochondrial accumulation in the axon terminal. Only after retrograde mitochondrial transport is inhibited does mitochondrial biogenesis fail, leading to loss of cell body mitochondria and decreases in the anterograde mitochondrial pool (summarized in Figure S4I).

Together, our data suggest that anterograde mitochondrial transport supplies the axon terminal with cell body-derived mitochondria produced through biogenesis. To test this, we directly stimulated mitochondrial biogenesis and analyzed axon terminal mitochondrial addition. To increase mitochondrial biogenesis, we used a stable transgenic zebrafish line overexpressing

human PGC-1α in neurons (*Tg(-5kbneurod1:PGC1α-2A-mRFP)*^{uwd9Tg}; [48]). PGC-1α overexpression in this line increased *tfam* expression in pLL neurons and has been previously shown to increase mitochondrial density in the axon terminal, confirming increased mitochondrial biogenesis (Figure S4J; [48]). To determine if increased mitochondrial biogenesis increases the addition of cell body-derived mitochondria to the axon terminal, we used photoconversion and mitochondrial tracking. For this, we used a dual transgenic line expressing PGC-1α ((*Tg(-5kbneurod1:PGC1α-2A-mRFP)*^{uwd9Tg}) and mEos, a photoconvertible protein, localized to the mitochondrial matrix (*Tg(-5kbneurod1:mito-mEos)*^{y586Tg}; [36,49]). We photoconverted the mitochondrial population in the pLL ganglion at 4 dpf and imaged axon terminals 4 hours post-conversion (hpc; Figure 3A). By 4 hpc, cell body-derived mitochondrial density in the axon terminal was significantly increased in PGC-1α transgenics, confirming that mitochondrial biogenesis in the cell body impacts mitochondrial addition to the axon terminal population (Figures 3B and C). Next, we assessed the density of cell body-derived mitochondria in *actr10* mutant axon terminals using the same photoconversion strategy. This demonstrated a 50% reduction in the contribution of cell body-derived mitochondria to the axon terminal population in *actr10* mutants (Figures 3B and C).

Reduced cell body-derived mitochondria in the axon terminal could be due to either fewer mitochondria or smaller mitochondria being transported to the terminal. To differentiate this, we tracked mitochondrial addition to the axon terminal using time-lapse imaging. Mitochondria in the pLL ganglion carrying matrix localized mEos were photoconverted and the axon terminal was imaged every minute for 6 hours (Movies S5 and S6). *actr10* mutants had both fewer and smaller cell-body derived mitochondria entering the terminal per hour (Figures 3D-F). Together, this suggests mitochondrial biogenesis in the cell body contributes to both number and size of new mitochondria transported to the axon terminal.

Disrupted mitochondrial fission does not alter mitochondrial biogenesis signatures

At the light microscopy level, mitochondria in *actr10* mutant pLL cell bodies have a more circular and aggregated morphology, suggesting impaired fission (see Figure 1B). To better understand the structure of pLL neuron cell body mitochondria, we used TEM to assess their ultrastructure in *actr10* mutants. In wildtype pLL cell bodies, mitochondria were evenly distributed throughout the cytosol (Figure S5A). In *actr10* mutants, cell body mitochondrial density and morphology were variable: some cell bodies had fewer but significantly enlarged mitochondria (Figure S5B; 5/12 cell bodies), some showed a more even distribution similar to wildtype (Figure S5C; 1/12), and some showed no visible mitochondria (Figure S5D; 6/12 cell bodies). In contrast, even wildtype cell bodies with little visible cytosolic area still had mitochondria present (Figure S5E; 0/10 cell bodies with no visible mitochondria). On average, mitochondria were significantly larger with a reduced number in *actr10* cell bodies (Figures S5F and G). Altered mitochondrial structure could suggest impaired mitochondrial health. However, previous work has shown *actr10* mutants have normal mitochondrial health measures in the cell body, and our TEM images show normal cristae even in the enlarged mitochondria (Figure S5B; [36]). Together, these data show that *actr10* mutant mitochondria are larger and rounder than those in wild type siblings, despite not showing altered measures of health and productivity [36].

Altered mitochondrial fission can result in large, circular organelles. Given the relationship between mitochondrial fission and mitochondrial biogenesis, we asked if disrupted mitochondrial fission in *actr10* mutants could underlie disrupted mitochondrial biogenesis [11,12].

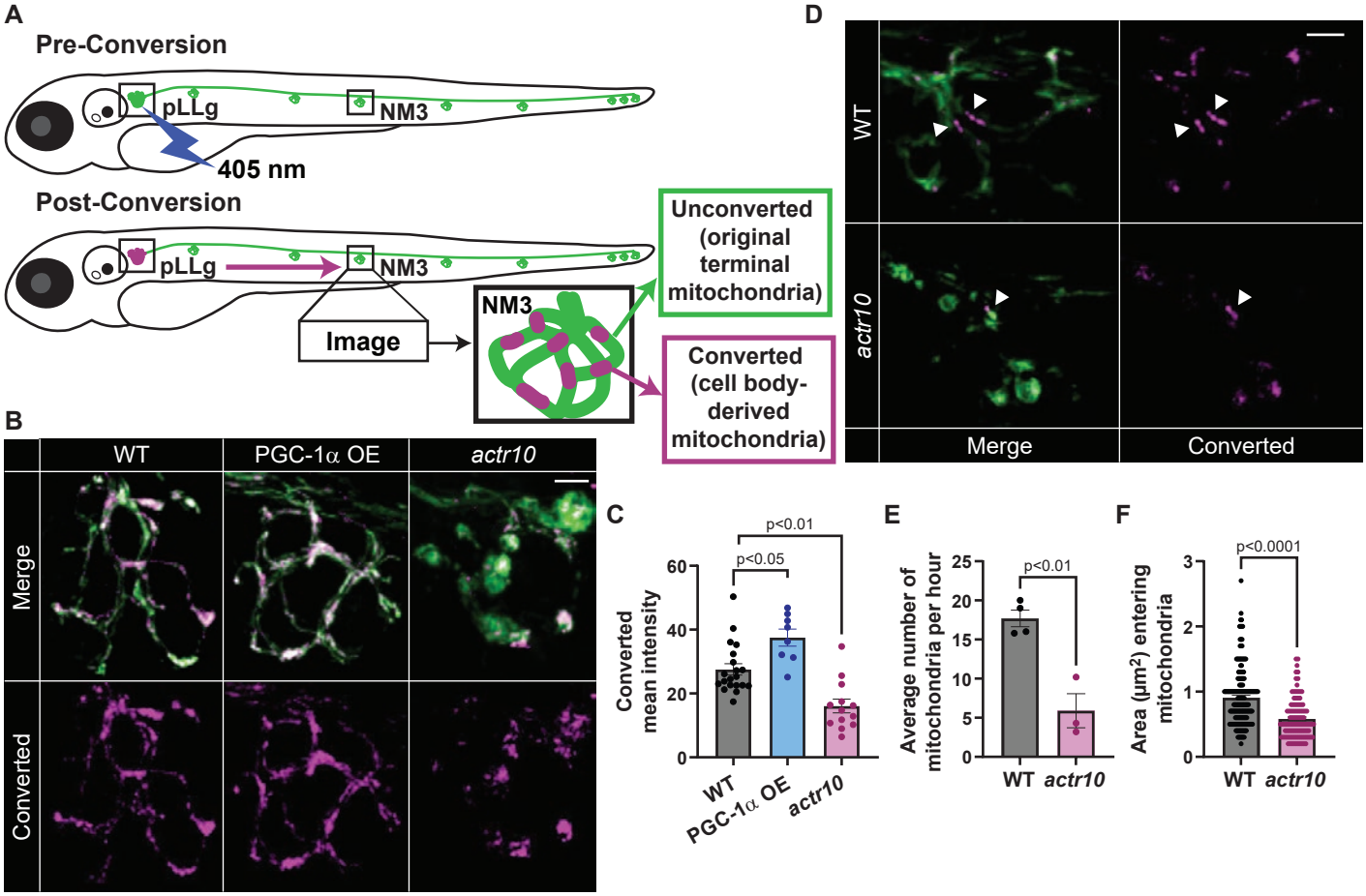

Figure 3: Cell body-derived mitochondrial density in the axon terminal is reduced in *actr10* mutants. (A) Photoconversion strategy. Mitochondrial matrix-localize mEos in the pLLg was locally converted using 405 nm laser. An axon terminal in the mid-trunk (neuromast 3 - NM3) was imaged 4 hpc (B) or every minute for 6h (D). (B) NM3 4 hpc in wild type, *actr10*, and transgenic overexpressing (OE) PGC-1α in neurons *(Tg(-5kbneurod1:PGC1α-2A-mRFP)^{unwd9})*. (C) Mean fluorescence intensity of cell body-derived mitochondria (Converted) in the axon terminal population (Steel-Dwass). (D) Representative timepoint of a pLL axon terminal from 6 hr timelapse video (Movies S5 and S6). Cell body-derived mitochondria indicated with white arrowheads. (E,F) Quantification of the number (E, ANOVA) and size (F, Wilcoxon) of converted mitochondria entering the axon terminal. Scale bars = 5 μm. All data are mean ± SEM. Data points represent individual larvae in C and E and individual mitochondria measured from 4 wild type and 3 *actr10* axon terminals in F.

First, we assessed length of moving and stationary mitochondria in pLL axons in *actr10* mutants and wild type siblings as a proxy for fission dynamics. These data showed no change in mitochondrial length, suggesting no change in fission or fusion dynamics in the axon (Figure S5H). The cell body mitochondria are too dense for us to directly measure their length or assess fission frequency. Instead, we disrupted mitochondrial fission and assessed measures of mitochondrial biogenesis. To disrupt mitochondrial fission, we expressed a dominant negative form of Drp1 which mimics a constitutively GDP-bound form of the enzyme ($Drp1^{K38A}$; [50,51]). In cultured cells, expression of $Drp1^{K38A}$ disrupts mitochondrial fission [50,51]. When expressed in pLL neurons, $Drp1^{K38A}$ causes clustering of mitochondria to the perinuclear region of the cell body and reduces mitochondrial density in both wild type and *actr10* cell bodies (Figures 4A and B). However, $Drp1^{K38A}$ expression does not change measures of mitochondrial biogenesis including *tfam* expression or the number of SSBP labeled replicating mtDNA nucleoids (Figures 4C-F). These data argue that loss of fission is not causal in the *actr10* mutant mitochondrial biogenesis phenotype.

MitoTruck mediated disruption of mitochondrial transport inhibits mitochondrial biogenesis

Our data demonstrate that inhibiting mitochondrial return to the cell body impairs mitochondrial biogenesis. To test this in another model, we engineered a synthetic tether, similar to one previously described in *C. elegans,* to constitutively move mitochondria out of the cell body and inhibit their ability to return to the cell body from the distal axon (MitoTruck; [52]). For this, we tethered mitochondria to a constitutively active kinesin motor domain derived from KIF1A using the OMP25 outer mitochondrial membrane localization sequence (Figure 5A; [53,54]). When expressed in pLL neurons, MitoTruck localizes to mitochondria and ectopically concentrates these organelles to axon ends, demonstrating anterograde transport bias (Figure 5B). Constitutive expression of MitoTruck caused failed axon extension and neuronal death by 4 dpf. To avoid any phenotypes due to failed neuronal health, we analyzed mitochondrial parameters after 24 hours of MitoTruck expression, at 2 dpf. Mitochondria in the cell body are significantly depleted in MitoTruck expressing neuron cell bodies by 2 dpf (Figures 5C and D). This depletion is similar to that observed in *actr10* mutants at 4 dpf (mitochondrial density: WT 2 dpf 0.57 ± 0.018, MitoTruck 2 dpf 0.33 ± 0.016, WT 4 dpf 0.55 ± 0.027, *actr10* 4 dpf 0.26 ± 0.028). Analyses of mtDNA replication and *tfam* expression demonstrated that MitoTruck significantly decreased these markers of mitochondrial biogenesis (Figures 5E-H). Together our *actr10* mutant and MitoTruck analyses demonstrate that inhibiting mitochondrial return to the cell body from the axon is sufficient to impair markers of mitochondrial biogenesis.

Estrogen-related receptors bridge mitochondrial transport with transcriptional regulation of mitochondrial biogenesis

Our data indicate retrograde transport is required to promote mitochondrial biogenesis through regulation of upstream factors including nuclear gene expression. Several nuclear transcription factors have been identified that bind the promoters of a wide range of mitochondrial genes, allowing for coordinated expression of these genes during biogenesis [10,55,56]. We hypothesized that a key transcription factor could link mitochondrial retrograde transport to mitochondrial biogenesis. To identify this transcription factor, we performed transcription factor enrichment analysis using significantly downregulated genes from our RNA-seq dataset. This in silico analysis identified Estrogen related receptors (ERRs) as top candidates (Figure 6A; Figure S6A). ERRs have been shown to be coactivated by PGC-1α to regulate mitochondrial biogenesis [55,57-59]. Other transcription factors regulated by PGC-1α such as NRF1/2 or PPARα were not found

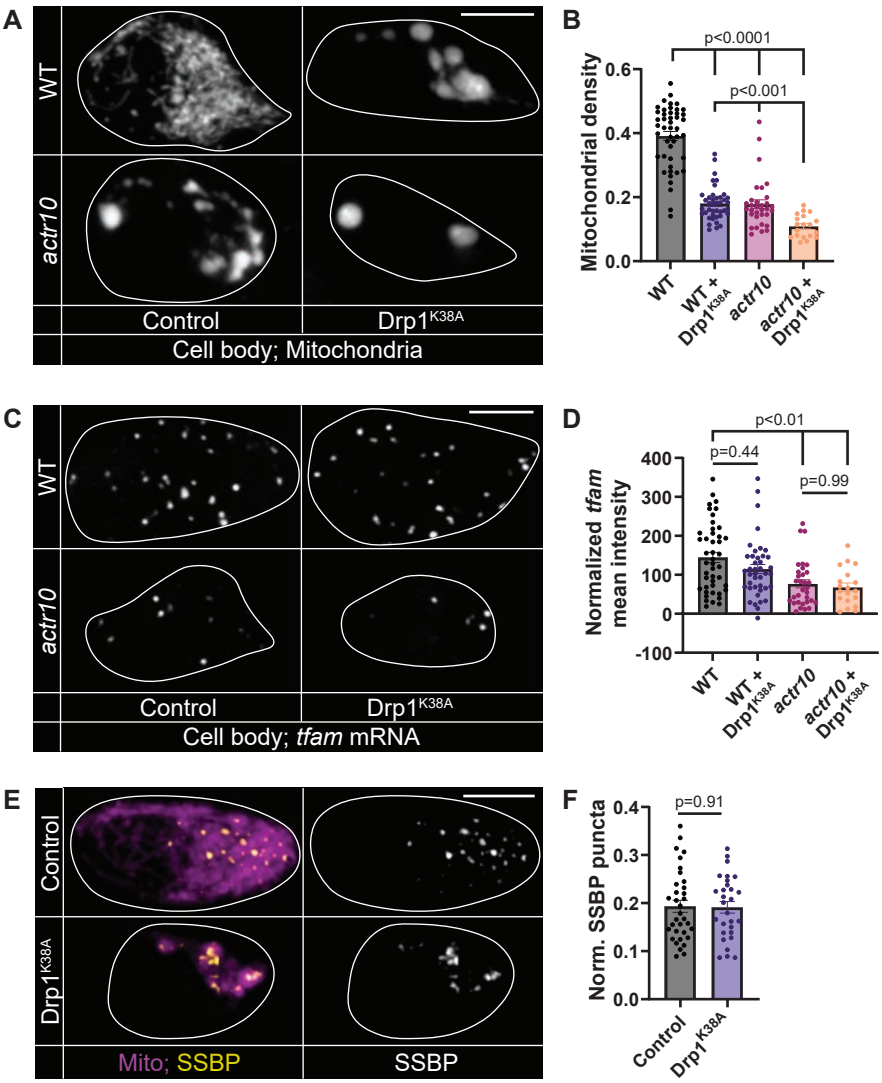

Figure 4: Disrupting mitochondrial fission does not alter *tfam* expression or mtDNA replication. (A) Single pLL cell bodies (white outline) expressing mitoTagRFP in wild type and *actr10* mutant larvae expressing Drp1^{K38A}-RFP or RFP (control). (B) Quantification of mitochondrial density (Steel-Dwass). (C) HCR RNA FISH labeling of *tfam* mRNA in a pLL cell body (white outline). (D) Mean fluorescence intensity of *tfam* (Steel-Dwass). (E) SSBP immunostaining in pLL cell body mitochondria, visualized with mitochondria-localized GFP (Mito, magenta). (F) Number of SSBP puncta normalized to mitochondrial volume (ANOVA). All data are mean ± SEM. Data points represent individual larvae.

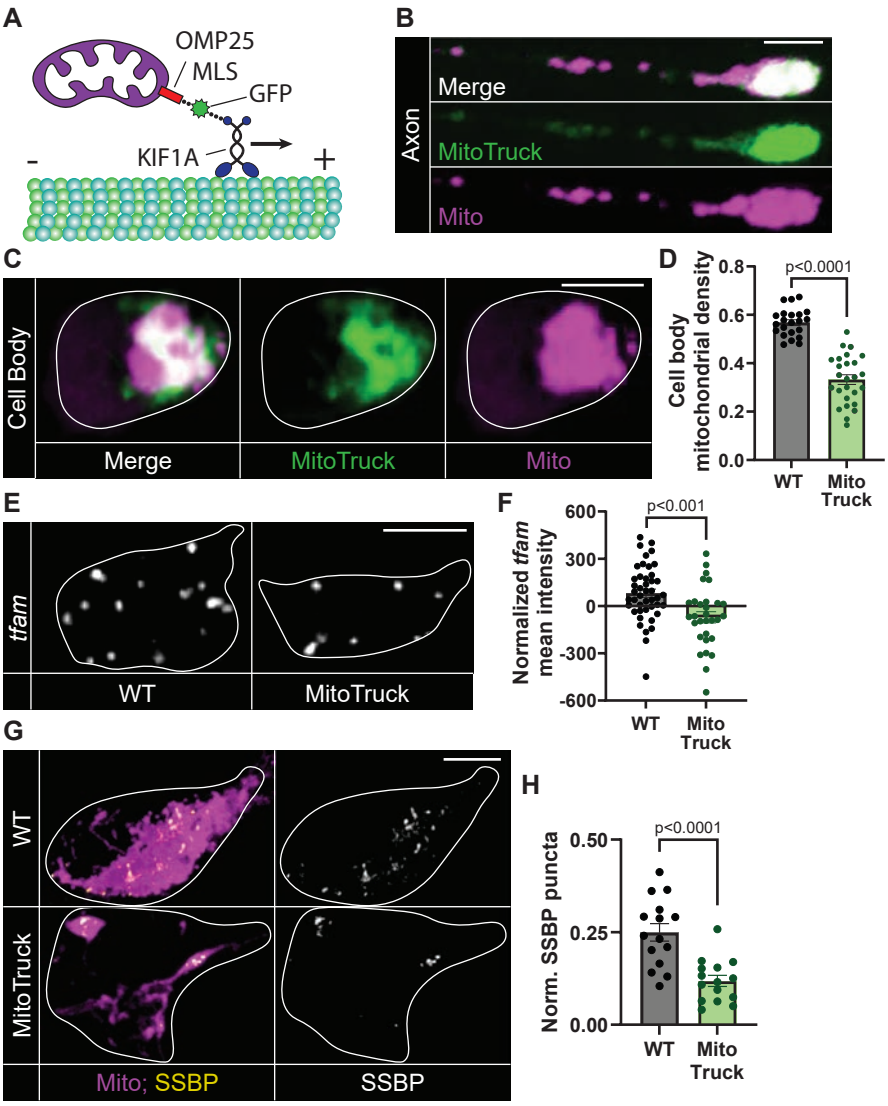

Figure 5: MitoTruck expression decreases cell body mitochondrial density and markers of mitochondrial biogenesis. (A) Schematic of the MitoTruck construct. The constitutively active KIF1A motor domain was tethered to mitochondria with the OMP25 outer mitochondrial membrane localization signal (MLS) and visualized with GFP. (B, C) pLL axon (B) and cell body (C) expressing MitoTruck (green) and MitoTagRFP (Mito, magenta). (D) Quantification of pLL cell body mitochondrial density (Wilcoxon). (E) Representative images of HCR RNA FISH labeling of *tfam* mRNA in a single pLL cell body (white outline) without and with MitoTruck expression. (F) Mean fluorescence intensity of *tfam* normalized to background (ANOVA). (G) SSBP immunostaining in a single pLL cell body. Mitochondria visualized with mitochondrially localized TagRFP (Mito, magenta). (H) Number of SSBP puncta normalized to mitochondrial volume (ANOVA). Scale bars = 5 µm. All data are mean ± SEM and points represent individual larvae.

to be enriched in our analysis, suggesting ERRs specifically may be affected in *actr10* mutants. To validate this result, we used gene set enrichment analysis of transcription factor binding targets and identified the ERR binding motif ERR1 enriched near downregulated genes (Figure S6B). Finally, we took a more targeted approach by comparing our list of downregulated genes to ESRRG targets identified by ChIP-seq in cultured neurons [59]. We found significant enrichment for known neuronal ESRRG target genes in our data set (Figure 6B). In contrast, there was only one target gene from the Chip-seq dataset that was significantly upregulated in our dataset (p=0.885, Fisher's exact test). Together, these in silico analyses suggest ERR-dependent transcription is reduced in *actr10* mutants.

If disruption of ERR-dependent transcription underlies decreased mitochondrial biogenesis in *actr10* mutant neurons, increasing ERR activity should rescue this defect. To test this, we overexpressed Esrra in pLL neurons and assessed mitochondrial density and biogenesis transcriptional programs. Similar to PGC-1α overexpression (see Figure S4J; [48]), Esrra overexpression significantly increased *tfam* expression (Figures 6C and D) and axon terminal mitochondrial density in wild type animals (Figures 6G and H), suggesting it can effectively upregulate mitochondrial biogenesis. Furthermore, Esrra overexpression in *actr10* mutants rescues *tfam* expression to wild type levels (Figures 6E and F) and can further elevate axon terminal mitochondrial density (Figures 6G and H), suggesting that loss of ERR signaling underlies loss of mitochondrial biogenesis in *actr10* mutants.

Activation of ERR-dependent transcription is modulated by ERR posttranslational modifications. The most well studied modifications that activate this pathway are SIRT1-dependent deacetylation of ERR and/or PGC-1α and AMPK-dependent phosphorylation of PGC-1α [60-64]. To determine if SIRT1 or AMPK activation were upstream of ERR-dependent mitochondrial biogenesis in neurons, we treated wild type and *actr10* mutant zebrafish with resveratrol (activator of SIRT1) or AICAR (activator of AMPK) at concentrations previously optimized for use in zebrafish larvae [60,65,66]. Resveratrol, but not AICAR, treatment was sufficient to rescue cell body mitochondrial load in *actr10* mutant neurons (Figures 7A-D). SIRT1 is activated by elevated NAD+ levels. A significant pool of cellular NAD+ is stored in mitochondria and changes to NAD+/NADH levels in mitochondria can affect the cytosolic pool [67-69]. We reasoned that altered mitochondrial transport could change local mitochondrial NAD+ levels, leading to a reduction in local SIRT1 activation in the cell body. To determine if changes to mitochondrial NAD+ could contribute to SIRT1 activation and subsequent mitochondrial biogenesis in *actr10* mutants, we assessed mitochondrial NAD+ in the cell body and axon terminal of pLL neurons using a genetically encoded NAD+ sensor [70]. Analysis of steady state NAD+ levels in the mitochondrial matrix demonstrated elevated NAD+ in the matrix of axon terminal mitochondria in *actr10* mutants while cell body mitochondria have a significant reduction in mitochondrial NAD+ levels (Figures 7E-G). Together, our data support a model in which the mitochondria with high levels of NAD+ returning to the cell body from the axon elevate local NAD+ levels to activate SIRT1-dependent ERR transcriptional activity necessary for sustained mitochondrial biogenesis in neurons (Figure 7H). We propose that disrupting retrograde mitochondrial transport locks mitochondria with high NAD+ in the axon terminal, blocking this critical signaling step for the positive regulation of mitochondrial biogenesis.

Discussion

Mitochondrial population maintenance is essential for neuronal health and function. These organelles are critical for a variety of functions including ATP production and calcium buffering,

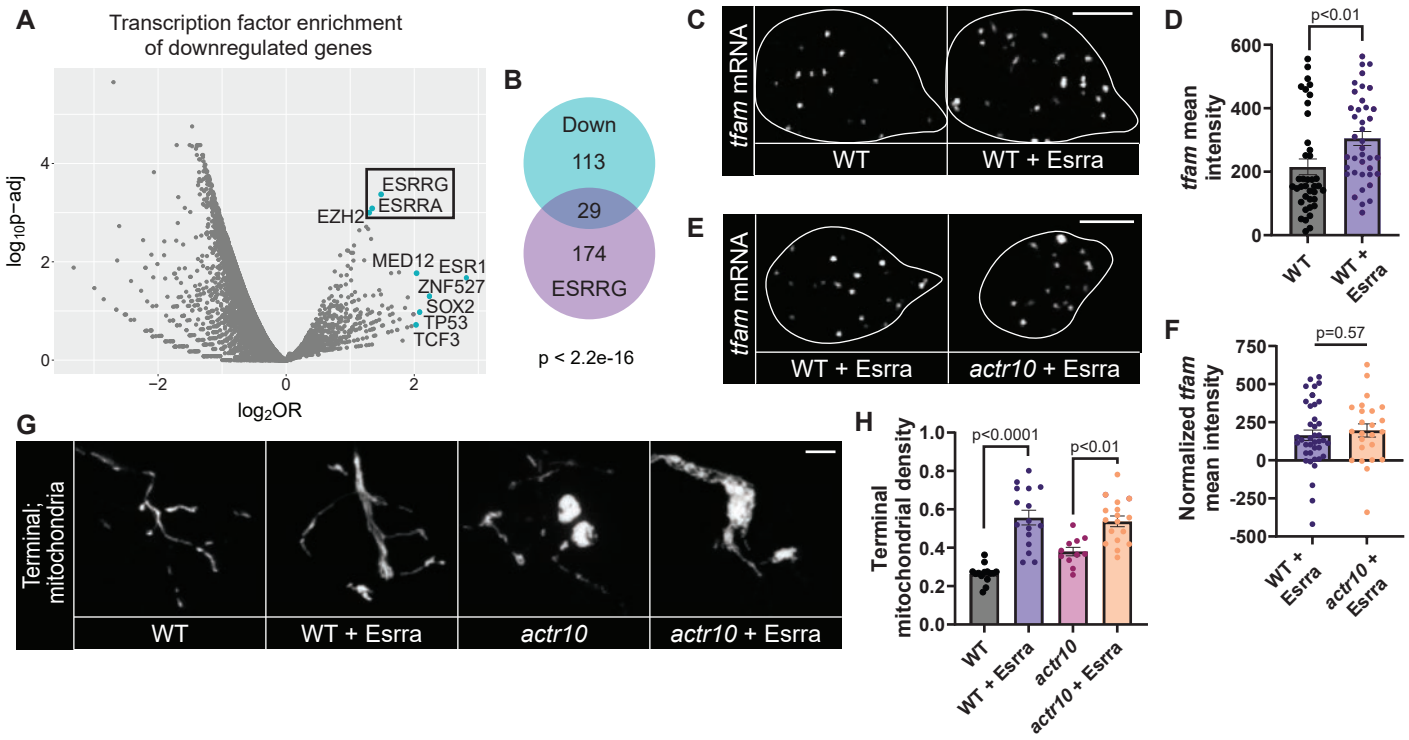

Figure 6: ERR activity links mitochondrial transport and mitochondrial biogenesis. (A) Transcription factor enrichment analysis for genes significantly downregulated in *actr10* mutants. Plot shows log2(Odds Ratio) vs. log10(adjusted p-value). Top 10 enriched genes based on euclidean distance from log2(OR)/log10(adj. p-value) to the origin are labeled. Box indicates ERR transcription factors identified in the dataset. (B) Overlap between downregulated genes and ESRRG neuronal ChIP-seq targets (Fisher's exact test). Human homologs of downregulated zebrafish genes were used for transcription factor analyses. Duplicated zebrafish paralogues were only counted once in the analysis. (C) HCR RNA FISH labeling of *tfam* mRNA in a pLL cell body (white outline) over-expressing (OE) Esrra and an adjacent control cell body in the same pLLg (WT). (D) Mean fluorescence intensity of *tfam* (paired t-test). (E) HCR RNA FISH labeling of *tfam* in a single pLL cell body (white outline) of a wild type and *actr10* larva overexpressing Esrra. (F) Mean fluorescence intensity of *tfam* normalized to background (ANOVA). (G) Mitochondria labeled by MitoTagRFP or Mito-eGFP in wild type and *actr10* axon terminals with and without Esrra overexpression. (H) Quantification of mitochondrial density (Steel-Dwass). (D, F, H,) Data points represent individual larvae; data are mean ± SEM. Scale bars = 5 µm.

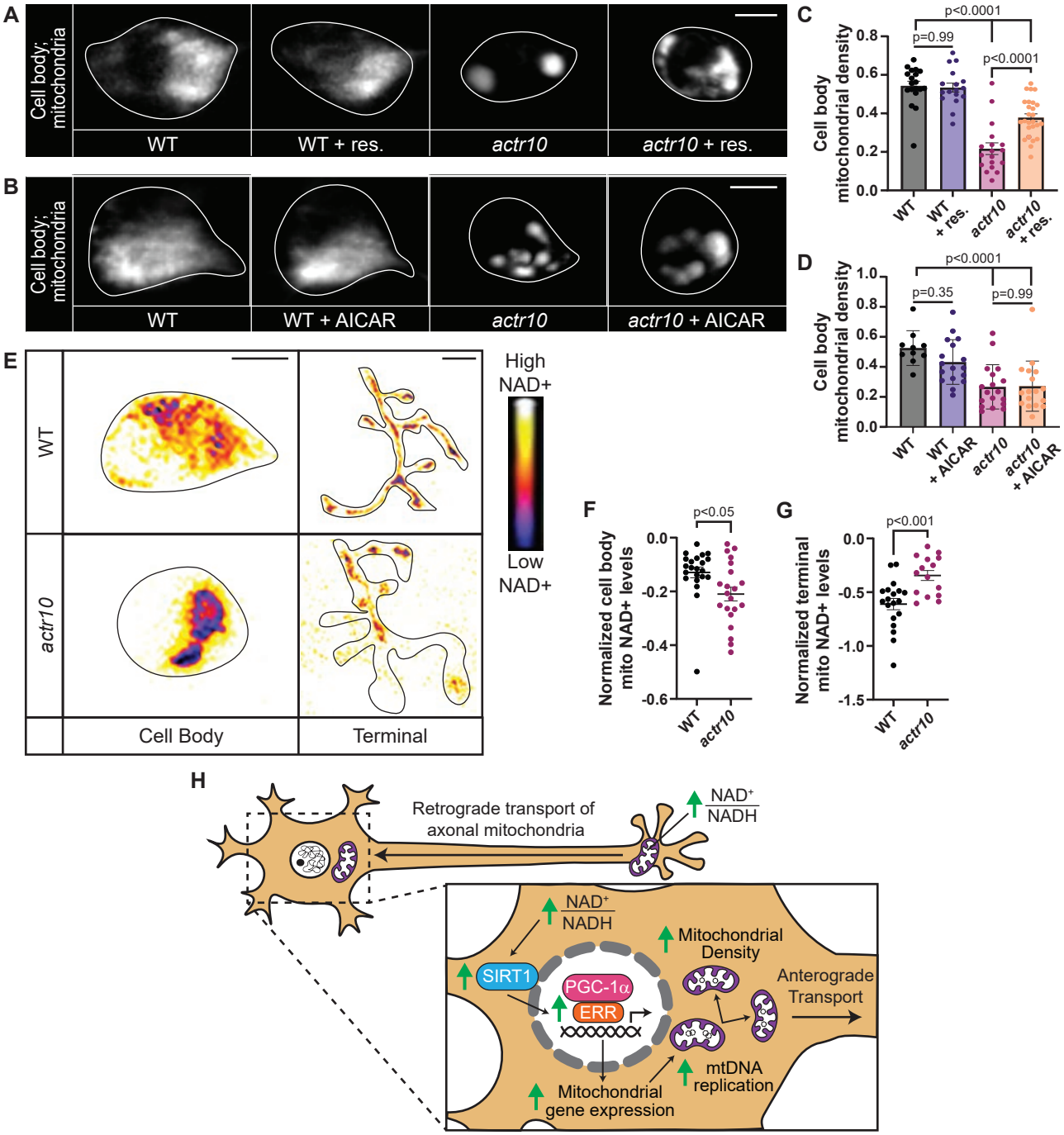

Figure 7: Activation of Sirt1 rescues cell body mitochondrial density. (A, B) Mitochondria in wild type and *actr10* pLL cell bodies with and without resveratrol (+ res.; A) or AICAR (+AICAR; B) treatment. (C,D) Quantification of mitochondrial density (ANOVAs; Tukey HSD). (E-G) Cell body and axon terminal mitochondrial NAD+ levels are altered in *actr10* mutants (cell body: Wilcoxon; axon terminal: ANOVA). Inverted heat map indicates levels of mitochondrial NAD+. Outline surrounds single pLL cell body and axon terminal. (H) Model of mitochondrial retrograde transport regulation of mitochondrial biogenesis. Data are mean ± SEM. Data points represent individual larvae. Scale bars = 5 µm.

particularly in axon terminals [1,2]. Through these functions, mitochondria accrue damage. Damaged organelles must be replaced through the process of mitochondrial biogenesis. Markers of mitochondrial stress such as an increased AMP/ATP or NAD+/NADH ratio as well as increased cellular calcium can activate mitochondrial biogenesis transcriptional programs in the nucleus [3-5,56,69,71,72]. However, it was unclear how these cellular signals could be transmitted long distances in the neuron to monitor mitochondrial populations in more distal regions of the neuron like the axon terminal. We identified a required role for retrograde return of axonal mitochondria to the cell body to sustain mitochondrial biogenesis transcriptional programs. We show that the return of axonal mitochondria to the cell body stimulates ERR-dependent nuclear gene transcription to regulate expression of mitochondrial genes, mtDNA replication, and ultimately increase mitochondrial biomass in the neuron. This provides a novel mechanism by which mitochondria in more distal regions of the neuron like the axon terminal can communicate with the nucleus to regulate mitochondrial density and mitochondrial population turnover in neurons.

The estrogen-related receptors (ESRRA, ESRRB, and ESRRG) are a family of orphan nuclear receptors first identified due to sequence similarity with estrogen receptors [73-75]. The three ERR proteins bind the ERR response element (ERRE) which is found in the promoter of many mitochondrial genes [55,75]. Because of this, increased ERR activity is associated with increased mitochondrial biogenesis in a number of tissues, including neurons [57,58,76,77]. Despite their similarity to estrogen receptors, ERRs do not have the capacity to bind estrogen, but rather are thought to be constitutively active [78]. Their activity can be regulated through expression level, post-translational modifications (PTMs), or interaction with co-activators like PGC-1α [8,9,76]. PGC-1α regulates ERR transcription and also interacts with ERRs as a coactivator to induce the transcription of mitochondrial biogenesis genes [8,9,58].

ERRs serve as mediators between mitochondrial signals and biogenesis transcriptional programs. In non-neuronal cells, signs of mitochondrial depletion or failed health like reduced cellular energy or increased cytosolic calcium have been shown to activate ERR-dependent transcription, either directly or through PGC-1α activation [13,79]. These upstream signals of cellular and mitochondrial health act through enzymes that can directly modify ERR and PGC-1α via PTMs including phosphorylation and acetylation. Two of the most well studied upstream regulatory factors are AMPK and SIRT1, which serve as energy sensors for the cell [6]. AMPK is activated by an increased AMP to ATP ratios and can activate mitochondrial biogenesis through PGC-1α phosphorylation [4,80]. SIRT1 is activated by an increased NAD+ to NADH ratio and can activate mitochondrial biogenesis through PGC-1α and/or ERR de-acetylation [3,63]. AMPK and SIRT1 can be artificially activated through AICAR and resveratrol treatment, respectively, to induce mitochondrial biogenesis [60,61,65,80,81]. In our experiments, resveratrol, but not AICAR, treatment was able to rescue *actr10* biogenesis defects. This suggests retrograde transport of axonal mitochondria may stimulate ERR-dependent mitochondrial biogenesis through activation of SIRT1, though we cannot rule out other upstream modulators which could function with SIRT1 in this process.

SIRT1 requires NAD+ as a co-substrate for the removal of acetyl groups from lysines, making NAD+ levels a direct regulator of SIRT1 enzymatic activity [82]. Increased NAD+ levels have been shown to increase SIRT1-mediated de-acetylation of PGC-1α, increasing its transcriptional activity [71,81]. Therefore, local NAD+ levels are a likely signaling mechanism by which non-neuronal cells are able to sense energy levels and respond with transcriptional regulation of mitochondrial biogenesis. However, it was unclear how the predominantly nuclear-localized

SIRT1 could sense and respond to levels of NAD+ in mitochondrial populations spread throughout the expansive dendritic and axonal arbors of neurons [83]. Our data suggests that retrograde transport is required to move mitochondria with high levels of NAD+ to the cell body to stimulate biogenesis. We show axon terminal mitochondrial NAD+ levels are increased while cell body mitochondrial NAD+ levels are reduced when retrograde transport of mitochondria is impeded. Based on this, we propose that local SIRT1 activity in the cell body requires increases in the local NAD+ levels which is accomplished by the movement of mitochondria with elevated NAD+ from the axon back to the cell body. Consequent activation of SIRT1 in the cell body then promotes mitochondrial biogenesis through de-acetylation of transcriptional regulators like PGC-1α or ERRs. In support of this, treatment with resveratrol, which circumvents the requirement for NAD+, can rescue mitochondrial density in *actr10* mutant cell bodies. It is likely that additional energy sensing pathways work with NAD+/SIRT1 to control mitochondrial biogenesis through additional transcription factor PTMs. Further work on transcription factor PTMs and associated modulatory pathways will clarify the role of energy sensing through NAD+ and other signaling molecules on the control of mitochondrial biogenesis in neurons.

In conclusion, our work demonstrates that transport of mitochondria from the axon back to the cell body is a positive regulator of neuronal mitochondrial biogenesis through regulation of ERR-dependent gene transcription. Mitochondria derived from biogenesis in the neuronal cell body are critical for maintaining cell body mitochondrial density as well as the anterograde mitochondrial pool that supports the axon terminal mitochondrial population. Unsurprisingly, impaired mitochondrial biogenesis can diminish neuronal health and has been linked to diseases like Parkinson's and Alzheimer's diseases [84-87]. However, regulatory mechanisms that govern this critical process in the neuron remain poorly understood. Here we show that neurons in zebrafish larvae require mitochondrial retrograde transport for effective mitochondria-nuclear communication to regulate mitochondrial biogenesis through ERRs. This novel mechanism provides new insight into how neurons regulate mitochondrial population health and density in response to changing demands on the organelle in distal compartments.

Acknowledgments: We would like to acknowledge members of the Drerup lab and Dr. Samantha Lewis for thoughtful discussions of the work and critique of the manuscript. The constitutively active KIF1A motor domain construct was provided by Dr. Marvin Bentley. We would like to thank the University of Wisconsin Carbone Cancer Center Flow Cytometry Laboratory, supported by P30 CA014520, for use of its facilities and assistance with fluorescence activated cell sorting. We would like to thank Randall Massey and the University of Wisconsin School of Medicine and Public Health Electron Microscopy Facility for assistance with Transmission Electron Microscopy.

Funding:

National Institutes of Health grant R01NS124692 (CMD)

National Science Foundation grant DEG-2137424 (AEL)

National Institutes of Health grant T32GM007133 (University of Wisconsin-Madison Predoctoral Training Program in Genetics; AEL)

University of Wisconsin-Madison Office of the Vice Chancellor for Research (CMD)

Wisconsin Alumni Research Foundation (CMD)

Author Contributions:

Conceptualization: AEL, CMD

Data acquisition and analysis: AEL, CS, CMD

Funding acquisition: AEL, CMD

Writing – original draft: AEL

Writing – review & editing: CMD

Competing interests: The authors declare no competing interests.

Data and materials availability: All data and materials are available upon request from the corresponding author.

Materials and Methods

Zebrafish husbandry

All zebrafish (*Danio rerio*) work was done in accordance with the University of Wisconsin-Madison Institutional Animal Care and Use Committee guidelines. Adult zebrafish were kept at 28°C and embryos were spawned according to established protocols [88]. Embryos and larvae were kept in embryo media (995 µM MgSO4, 154 µM KH2PO4, 42 µM Na2HPO4, pH 7.2, 1.3 mM CaCl2, 503 µM KCl, 15 mM NaCl, 714 µM NaHCO3), maintained at 28°C, and developmentally staged using established methods [89]. All experiments were performed at 4 dpf unless otherwise specified. Sex is not determined at this stage. Zebrafish strains used for these experiments are listed in Table 1. The Tg(*hsp70l:EGFP-en.sill*)^{uwd12} transgenic was derived using Tol2-mediated transgenesis and the *hsp70:eGFP-SILL* plasmid as described [90]. Genotyping for *actr10*^{nl15} [34], *p150a*^{y625} [36], *p150b*^{nl16} [34], and *nudc*^{nl21} [43] was done as previously described using the primers in Table 2.

Cloning

The DNA expression plasmids used in this paper are listed in Table 1. Novel DNA expression constructs were constructed using Gibson cloning with oligonucleotides listed in Table 2 [91]. *5kbneurod1:kif1a-egfp-omp25* ["MitoTruck"] was created using the zebrafish outer membrane protein 25 (OMP25) mitochondrial localization sequence (MLS) cloned from 4 dpf zebrafish cDNA. The truncated constitutively active rat ortholog of KIF1A was cloned from *pBA-kif1a393-tdTomato-FKBP* [92]. *5kbneurod1:cox8a-cox8a-halotag* was created by fusing two copies of the cox8a MLS to a HaloTag using the oligos listed in Table 2. *5kbneurod1:esrra-p2a-mRFP* was created using the zebrafish *esrra* sequence derived from 4 dpf zebrafish cDNA and existing p2a and mRFP plasmids using the oligos specified in Table 2 [90]. *5kbneurod1:cox8a-cox8a-NAD-p2a-RFP* was created from plasmids containing a double cox8a MLS, a NAD+ biosensor (gift of Michael Cohen: Addgene plasmid 186791; [70]), and a p2a-RFP using the oligos listed in Table 2. The NAD+ biosensor consists of a circularly permuted Venus fluorescent protein (cpVenus) with a bipartite NAD+-binding domain modeled from bacterial DNA ligase [70]. *5kbneurod1:cox8a-cox8a-paGFP-p2a-mitoTagRFP* was created from plasmids containing a double cox8a MLS, a photo-activatable GFP, and a p2a-mitoTagRFP using the oligos listed in Table 2. *hsp70l:EGFP-en.sill* was created using existing plasmids containing the hsp70 minimal promotor, eGFP, and the 3' SILL enhancer element that limits expression to the pLL ganglion using oligos specified in Table 2 [90,93]. For all expression plasmids except the *hsp70* driven construct, expression was controlled by a 5kb portion of the *neurod* promotor as previously described [90,94]. All novel DNA expression plasmids were sequenced and verified prior to use.

Live imaging acquisition and analysis

For live imaging of pLL neurons, we used a combination of transient transgenesis and stable transgenic expression. For transient transgenesis, 3-25 pg of plasmid DNA was microinjected into zebrafish zygotes as previously described [34,95,96]. Plasmids used for these experiments are listed in Table 1. For imaging, zebrafish larvae were sorted to identify larvae with expression in a subset of pLL neuron cell bodies using an AxioZoom V.16 Zeiss microscope. For HaloTag constructs, larvae were treated with Janelia Fluor 635 in embryo media at 1 μM for 1-2 h or 0.1 μM overnight at 28.5°C in the dark. For all live imaging, larvae were anesthetized in 0.02% tricaine, mounted in 1.5% low melt agarose in embryo media, and imaged with an Olympus FV3000 confocal microscope with a 40x (NA 1.25) silicone oil objective. Optimal interslice interval was used for all imaging.

Larval TgBAC(*neurod:egfp*)^{nl1} transgenic zebrafish image (Figure 1A) was created by stitching overlapping regions of the larvae imaged using the Olympus FV3000 with a 10X objective using the pairwise stitching plugin in ImageJ [97,98]. Non-linear adjustment to midtones to show the full nervous system was done using the levels function in Adobe Photoshop. A brightfield image of the full larva was taken using the AxioZoom V.16 Zeiss microscope with a Zeiss Axio 506 color camera and overlaid using Adobe Photoshop with opacity adjusted to 10%.

To quantify mitochondrial density in the pLL cell body and axon terminal, area was measured from standard deviation z-projections in ImageJ. Mitochondrial area was measured using a manually applied threshold while cytosolic area was measured by manual tracing or applied threshold of a cytosolic fill. Mitochondrial density was calculated as mitochondrial area divided by cytosolic area. To quantify mitochondrial or cell volume, the 3D objects counter was used in ImageJ using a manually applied threshold [98].

Mitochondrial axonal transport analyses were done as described previously [96]. Briefly, transient transgenesis of *5kbneurod1:mitotagRFP* was used to visualize mitochondria in pLL axons. 30–100 μm lengths of axon were imaged as a single *z*-plane at a rate of 300 ms per frame for 1000 frames. Kymographs were generated using the ImageJ Multi Kymograph function [98]. Anterograde, retrograde, and bidirectional mitochondria number were quantified using kymographs while stationary mitochondria number was quantified by visual analysis of transport videos. Mitochondrial length was manually measured from transport movies using the line selection tool in ImageJ.

For NAD+ quantification, *5kbneurod1:cox8a-cox8a-NAD-p2a-RFP* was transiently expressed in pLL neurons by zygotic microinjection. For imaging, larvae were mounted live as described above and cell body and axon terminal regions were imaged at 4 dpf with consistent laser power and detector gain for all images. For analysis, cell body and axon terminal regions were isolated using the mRFP cytosolic signal as a mask and the image subtraction function in ImageJ [98]. cpVenus and mRFP mean fluorescence intensity were then quantified from sum projections of the isolated region. For analysis, mean fluorescence intensity of cpVenus was normalized to mean fluorescence intensity of RFP to control for differences in expression level. NAD+ binding to the bipartite NAD+-binding domain in the biosensor decreases cpVenus fluorescence intensity in a dose-dependent manner [70]. The images in Figure 7E-G were generated using the fire lookup table in ImageJ and the images/data are inverted to appropriately reflect the direction of change in NAD+ levels.

<u>Drug treatment</u>

Resveratrol and AICAR (5-aminoimidazole-4-carboxamide ribonucleotide) stocks (200 mM and 27.5 mM respectively) were diluted in embryo media to concentrations previously shown to be

effective in larval zebrafish (Resveratrol 300 μM, AICAR 1 mM; [66]). At 3 dpf, transient transgenic larval zebrafish expressing cytosolic GFP and mitochondrially localized tagRFP (see Table 1 for DNA constructs) were placed in a 6 well plate and incubated overnight (18-24 h) in drug or equal amount of drug solvent (DMSO for resveratrol, sterile H_2O for AICAR) in embryo media. After treatment, larvae were mounted live, pLL neuronal cell bodies were imaged, and mitochondrial density analyzed as described above.

Heat shock-induced expression of Drp1^{K38A}

Hsp701:Drp1K38A-mRFP [34] or *5kbneurod1:RFP* [34] (control) was transiently expressed in pLL neurons with *5kbneurod1:mito-eGFP* in pLL neurons by zygotic microinjection as described [96]. At 4 dpf, larvae of both groups were placed in PCR strip tubes (2-3 larvae per tube) with approximately 200 μl of embryo media. Larvae were incubated at 37°C for 1 hour in a PCR machine (BioRad) then returned to 28°C. Larvae were fixed in 4% paraformaldehyde 7 hours post-heat shock for subsequent analysis.

Photolabeling

5kbneurod1:cox8a-cox8a-paGFP-p2a-mitoTagRFP was transiently expressed in pLL neurons by zygotic microinjection as described [96]. Cell body or axon terminal mitochondrial-matrix localized PA-GFP was specifically photoactivated by illuminating with a 405 nm laser using a region of interest (ROI) defined around the structure. For each larva, a pre-activation image was taken (488 nm and 561 nm lasers), the region was scanned for 1 to 5 seconds with 1% 405 nm laser power using the stimulation function for conversion, and a post-activation image (488 nm and 561 nm lasers) was taken to confirm activation. The axon terminal was then re-imaged at set timepoints post-conversion. PA-GFP and MitoTagRFP mitochondrial area were quantified as described earlier. "Proportion original mitochondria" for terminal activation and "proportion of cell body-derived mitochondria" for cell body activation was quantified as PA-GFP area/MitoTagRFP area (see Figure S3).

Photoconversion of mitochondrially localized mEos was performed using the stable transgenic *Tg(-5kbneurod1:mito-mEos)*^{y586Tg} as previously described [36]. The pLL ganglion was specifically converted by illuminating with a 405 nm laser through a z-stack of the entire ganglion with regional restriction using a region of interest (ROI) defined around this structure. For each larva, a preconversion image was taken (488 nm and 561 nm lasers), the stack was scanned with 1% 405 nm laser power for conversion, and a postconversion image (488 nm and 561 nm lasers) was taken to confirm complete green to red conversion of mEos in pLL cell bodies. For 4 hour timepoint analysis, the axon terminal of a sensory organ in the center of the trunk (NM3) was imaged 4 hours post pLL ganglion conversion. All microscope settings were kept consistent for all images. For axon terminal analysis, the red and green channels were merged and a mask was created by thresholding a standard deviation projection of the axon terminal *z*-stack. The mask was applied to a sum projection of the red channel and mean fluorescence was quantified. For timelapse analysis, a z-stack through an ROI surrounding NM3 was scanned minute for 6 hours. Image analysis was performed by manually scanning through standard deviation z-stack projections from the time series. Cell body derived (red photoconverted) mitochondria were counted and area was measured by manual outlining in ImageJ.

In situ Hybridization and Hybridization Chain Reaction RNA Fluorescent In situ Hybridization (HCR RNA FISH)

Colorimetric in situ hybridization was done according to established protocols [95,99]. To generate probes for *in situ* hybridization, we amplified 200-600 base pair regions of relevant cDNA within the open reading frames of genes of interest to use as a template for probe synthesis ([100]; Table 2). Zebrafish were fixed overnight in 4% paraformaldehyde (PFA) in phosphate-buffered saline (PBS) at 4°C. Fixed larvae were washed in PBS/0.1% Tween-20 and dehydrated in a methanol series. Larvae were stored in methanol at -20°C. Larvae were rehydrated with PBS/0.1% Tween-20 in a reverse methanol series. Larvae were treated with 10 µg/ml proteinase K in PBS/0.1% Tween-20 for 15 minutes then immediately fixed for 20 min in 4% PFA at room temperature (RT). Larvae were washed with PBS/0.1% Tween-20 then prehybridized for 1-2 hours at 65°C. Larvae were incubated overnight at 65°C with probe diluted 1:200 in hybridization buffer (10 mM citric acid, 0.1% Tween-20, 50 µg/ml heparin, 5× saline sodium citrate (SSC), 50% formamide). Larvae were washed at 65°C with a hybridization buffer-SSC buffer series (2:1 buffer:2x SSC 15 min; 1:2 buffer:2x SSC 15 min; 2x SSC 15 min; 0.2x SSC 30 min twice). Larvae were then washed at RT with 2:1 and then 1:2 0.2x SSC:PBS/0.1% Tween-20 for 5 min. Larvae were blocked in block solution (2% goat serum, 10% bovine serum albumin in PBS/0.1% Tween-20) for 2 hours at RT, and then sheep anti-digoxigenin (1:10,000) in block solution overnight at 4°C. Larvae were washed 6 times 15 min in PBS/0.1% Tween-20, 3 x 5 min in coloration buffer (100 mM Tris–HCl pH 9.5, 50 mM MgCl2, 100 mM NaCl, 0.1% Tween-20), then stained with 0.45% nitro blue tetrazolium, 0.35% 5-bromo-4-chloro-3-indolyl phosphate in a coloration buffer in dark until color development. Larvae were washed with PBS/0.1% Tween-20, fixed for 20 min in 4% PFA at RT, dehydrated in a methanol series, and rehydrated for imaging and sorting of RNA expression. WT and *actr10* mutant zebrafish were kept in the same tube for processing, then blindly sorted based on RNA expression into two groups (high and low expressing). Representative larvae were mounted in 1.5% low melt agarose in embryo media and imaged with a Zeiss Axio Imager.M2 microscope with Zeiss Axio 506 color camera. Sorted larvae were genotyped using the oligonucleotides in Table 2.

HCR RNA FISH was performed as described previously [48]. An mRNA transcript-specific probe set for each gene of interest was designed by Molecular Instruments (Table 3). Larvae fixation, methanol dehydration/rehydration, and Pro K treatment were performed as described for colorimetric in situ hybridization with modification in the Pro K treatment for larvae less than 4 dpf. 2 dpf larvae were treated with Pro K for 5 min, 3 dpf for 10 min, and 4 dpf for 15 min, followed by post-fixation. Larvae were incubated with a manufacturer-supplied hybridization buffer at 37°C for 1 h and then incubated in 4 nM (*pgc1a* and *tfam*) or 16 nM (others) probe in hybridization buffer at 37°C overnight. Larvae were washed with a manufacturer-supplied wash buffer and then SSC/0.1% Tween-20. Then, larvae were incubated in a manufacturer-supplied amplification buffer at RT for 30 min, during which manufacture-supplied reporter-labeled fluorescent hairpins were individually heated at 95°C and then cooled to RT for 30 min in the dark. Larvae were placed in fresh amplification buffer with 60 nM hairpins. B1 probes were labeled with 546 nm wavelength hairpins while B2 probes were labeled with 647 nm wavelength hairpins combined in the same tube. Larvae were incubated overnight in the dark at RT. Larvae were mounted between glass slides and #1.5 coverslip with Fluoromount mounting medium prior to imaging with an Olympus FV3000 confocal microscope with a 60x (NA1.42) oil objective. For each probe, laser power and detector gain were kept consistent for all images.

To quantify HCR signal in the whole pLL ganglion in *TgBAC(neurod:eGFP)*^{nl1} larvae, a mask was created using the GFP channel threshold using the default auto thresholding algorithm in ImageJ and the image subtraction function was used to remove non-neuronal signal. After using

the mask to exclude signal outside the pLLg, a sum projection of the probe signal was created and mean fluorescence intensity was measured. To quantify HCR signal in single cell bodies, a substack was created around the cell of interest and a sum intensity z-projection of the probe signal was created. The cell body was manually outlined and mean fluorescence intensity of the probe signal within the cell body was measured. To quantify background signal, a region outside the pLLg or cell body was selected and the sum intensity of probe signal was measured. Background mean signal was subtracted from pLL mean signal to get the normalized mean fluorescence intensity.

Immunolabeling

For SSBP and TFAM immunolabeling, transient transgenesis of either *5kbneurod1:mito-eGFP* or *5kbneurod1:mitotagRFP* was used to localize pLL cell body mitochondria. Larvae were fixed in 4% PFA/0.25% Triton X-100 at 4°C overnight then incubated in water at RT overnight. Larvae were kept in block (0.1% Triton X-100, 1% dimethyl sulfoxide, 0.02% sodium azide, 0.5% bovine serum albumin, 5% goat serum) at RT for 2h, then incubated with antibody in block overnight at 4°C. Larvae injected with *5kbneurod1:mito-eGFP* were incubated with chicken anti-GFP (1:2000) to amplify signal. Larvae were incubated with either rabbit anti-SSBP1 (1:500) or rabbit anti-TFAM (1:100). Larvae were then washed in PBS/0.1% Triton X-100 before incubation in goat anti-chicken AlexaFluor 488 (1:1000) and goat anti-rabbit AlexaFluor 568 (1:1000) or goat anti-rabbit AlexaFluor 647 (1:1000) at 4°C overnight. Larvae were washed in PBS/0.1% Triton X-100 prior to imaging as described for HCR. For analysis, a mask was created from the mitochondrial channel using the default auto thresholding algorithm in ImageJ and the image subtraction function was used to remove signal outside the pLL cell body. For TFAM quantification, the 3D objects counter function in ImageJ and manual thresholding was used to quantify volume of TFAM puncta and mitochondria (mitochondrial volume used for normalization). For SSBP1 quantification, SSBP1 puncta were manually counted and normalized to mitochondrial volume.

Transmission Electron Microscopy

4 dpf wild type and *actr10* mutant larvae samples were dissected by removing the trunks posterior to the pLLg and then fixed in Karnovsky's fixative (2.5% glutaraldehyde/2.0% formaldehyde in 0.1M NaPO4 buffer (PB), pH=7.2) at 4°C overnight. All remaining steps were performed on the specimens in glass scintillation vials on a rotator unless specified. The fixative was removed and the samples washed 5 x 5 min in PB at RT. Post-fixation was performed on the samples in 1% OsO4 in PB for 1 hour at RT. The samples were again washed in PB, 7 x 5 minutes at RT. Dehydration was performed with a graded series of EtOH (35%, 50%, 70%, 80%, 90% 5 x 5 minutes, 95% for 10 minutes, 100% for 3 x 10 minutes) at RT. Specimens were transitioned from EtOH by rinsing 2 x 7 minutes in acetone at RT. Samples were infiltrated and embedded in EMBed 812 resin (EMS Hatfield; PA 19440) using a graded series of 2:1 Acetone / EMBed812 1 hour RT, 1:1 Acetone / EMBed812 overnight RT, 1:2 Acetone / EMBed812 2 hours RT. 100% EMBed 812 resin infiltrations continued in uncapped vials for 1 hour at 65ºC in a laboratory microwave, with a fresh change of resin for 1 hour at 75ºC. Final embedding was done in EMBed 812 resin in aluminum weighing dishes placed in a 60ºC drying oven and allowed to polymerize for 2 days. Polymerized samples had the aluminum dishes stripped, with the target specimen area sawed out with a jewelers saw and glued to blank polymerized stubs of EMBed 812 resin. Specimens were sectioned on a Reichert-Jung Ultracut E ultra-microtome with sections collected on formvar coated, Cu 2x1 slot grids. Grids were post-stained in uranyl

acetate and Reynolds lead citrate and viewed on a Philips CM120 at 80kV. Images were collected on a BioSprint12 digital camera. One section of the pLLg was imaged for a WT and *actr10* mutant larvae. All cells visible within the section were analyzed. Images were calibrated in ImageJ and analyzed by manual counting of mitochondria and manual outlining for mitochondrial, cell, and nuclear area. Cytosolic area was calculated as cell area minus nuclear area.

Western blot

Western blot of TFAM and SSBP protein was done as described previously [34]. Protein lysates of 4 dpf wildtype larvae were run on a 12% sodium dodecyl sulfate polyacrylamide electrophoresis gel. After transfer to the polyvinylidene difluoride membrane, the blots were blocked in 5% nonfat dry milk in 1X PBS/0.1% Tween for 1–4 hours before incubation with anti-TFAM (1:1000) or anti-SSBP1 (1:500) overnight in block at 4°C. Membranes were then washed in 1X PBS, 0.1% Tween20 and incubated with secondary antibody conjugated to horseradish peroxidase for 90 min at RT. The blot was developed with a Western Sure Chemiluminescent Substrate (LiCor) on a C-DiGit Blot Scanner.

Embryo dissociation and fluorescence activated cell sorting (FACS)

20-30 4 dpf *Tg(hsp70:eGFP-SILL)*^{uwd12} larvae were collected in 1.5 ml microcentrifuge tubes. Embryo media was removed and larvae were incubated in 100 µL sterile, calcium-free ringer's solution (116 mM NaCl, 2.6 mM KCl, 5 mM HEPES pH 7.0) at RT for 5 min. 600 µL of sterile protease solution (0.25% trypsin, 1 mM EDTA, pH 8.0, PBS) was warmed to 28°C and 27 µl of Collagenase P (100 mg/mL in HBSS) was added to the tube and mixed. Larvae were incubated at 28°C. Every 30s, larvae were homogenized for 30s by pipetting first with a P1000 pipette until partially dissociated, then with a P200 pipette until fully dissociated. Once dissociated, 100 µl of sterile stop solution (30% calf serum, 6 mM CaCl2, PBS) was added and mixed. The cells were spun down at 350xg at 4°C for 5 min. The supernatant was removed and replaced with 500 µl sterile suspension solution (1% FBS, 0.8 mM CaCl2, 50 U/mL penicillin, 0.05 mg/mL streptomycin, DMEM) chilled to 4°C. Cells were spun at 350xg at 4°C for 5 min. The supernatant was removed and 500 µl of chilled sterile suspension solution was used to resuspend cells. Resuspended cells were passed through a 40 µm cell strainer into FACS tube and stored on ice until sorting. Immediately prior to sorting, DAPI (1:1000) was added to sort out dead cells. GFP+ DAPI- cells were sorted on a BD FACSAria™ III Cell Sorter with a 100 µm nozzle into 500 µL TRIzol LS in a 1.5 mL microcentrifuge tube.

Bulk RNA sequencing and analysis

Sorted pLL neurons were pooled into 3 replicates each for wild type and *actr10* samples. RNA was isolated using TRIzol. The SMART-Seq® v4 Ultra® Low Input RNA Kit was used for poly(A)+ selection, cDNA synthesis and amplification, followed by Illumina 150-bp paired-end sequencing performed by Azenta Life Sciences (South Plainfield, NJ). Sequence reads were trimmed to remove possible adapter sequences and nucleotides with poor quality using Trimmomatic v.0.36 [101]. The trimmed reads were mapped to the Danio rerio GRCz10.89 reference genome available on ENSEMBL using the STAR aligner v.2.5.2b [102]. Unique gene hit counts were calculated by using FeatureCounts from the Subread package v.1.5.2 [103]. Only unique reads that fell within exon regions were counted. Using DESeq2 [104], a comparison of gene expression between WT and *actr10* samples was performed. The Wald test was used to generate p-values and log2 fold changes. Genes with an adjusted p-value < 0.05 and absolute

log2 fold change > 1 were called as differentially expressed genes for each comparison. Alignment and differential expression analysis was performed by Azenta Life Sciences (South Plainfield, NJ).

KEGG pathway enrichment was performed for genes that were called as significantly upregulated or significantly downregulated using the ShinyGO (v0.82) webserver (*84-86*). *Danio rerio* gene IDs were used as input and background genes were defined as all genes that were detectable in the RNA-sequencing dataset. Default parameters were maintained. KEGG pathway plots were downloaded directly from the ShinyGO webserver. Gene Set Enrichment Analysis (GSEA) for differentially expressed genes was performed using the clusterProfiler R package with all gene ontology terms included, using the genome-wide annotation for Zebrafish (org.Dr.eg.db v3.19.1; [105]). Zebrafish gene IDs were converted to their closest human gene orthologues using the g:Profiler g:Orth webserver [106]. Fisher's exact test enrichment analysis was performed using the fisher.test function in R to test overlap between significantly upregulated or significantly downregulated genes and either the MitoCarta database or the ESRRG ChipSeq targets [47,59]. Transcription factor enrichment analysis was performed using the TFEA.ChIP webserver which uses information derived from the ChIP-seq datasets available from the ENCODE project, GEO Datasets, GeneHancer, ReMap 2018, and ReMap 2022 databases [107]. The significantly downregulated genes were used with background genes defined as all genes that were detectable in the RNA-sequencing dataset. Wilcoxon rank-sum was used for transcription factor ranking. Over-representation analysis of transcription factor target motifs was performed using the Webgestalt webserver with the functional database identified as ''network: transcription factor target" [108]. The significantly downregulated genes were used with background genes defined as all genes that were detectable in the RNA-sequencing dataset. Default parameters were maintained. Volcano plots of differentially expressed genes and transcription factor enrichment were created using the ggplot2 R package [109].

Experimental design, statistical analysis, and figure assembly

All image analysis was performed using ImageJ [98]. Statistical analysis was performed using JMP18 and data plots made using GraphPad Prism 10, unless indicated otherwise in the method section. Sample size estimated based on previous work and determined by power analyses. Imaging and analysis done blind to genotype, allowing inherent randomization and blinding to experimental condition. All experiments were replicated no less than two times (experimental replicates) with sample size for each experiment representing biological replicates. Statistical tests/post hoc analyses and other statistical details for each data set are indicated in the text or figure legends. For parametric data, ANOVAs were used with Tukey HSD post-hoc contrasts for multiple pairwise comparisons within a dataset. For nonparametric data, single comparisons were done using Wilcoxon/Kruskal-Wallis analysis, multiple comparisons using the Steel-Dwaas test. Images were created using ImageJ and linear adjustments to brightness/contrast were made equally for images being compared. Figures were compiled in Adobe Illustrator and supplemental movies were handled in Adobe After Effects.

References

1. Suomalainen, A., and Nunnari, J. (2024). Mitochondria at the crossroads of health and disease. Cell *187*, 2601-2627. 10.1016/j.cell.2024.04.037.

2. Misgeld, T., and Schwarz, T.L. (2017). Mitostasis in Neurons: Maintaining Mitochondria in an Extended Cellular Architecture. Neuron *96*, 651-666. 10.1016/j.neuron.2017.09.055.
3. Gerhart-Hines, Z., Rodgers, J.T., Bare, O., Lerin, C., Kim, S.-H., Mostoslavsky, R., Alt, F.W., Wu, Z., and Puigserver, P. (2007). Metabolic control of muscle mitochondrial function and fatty acid oxidation through SIRT1/PGC-1α. The EMBO Journal *26*, 1913-1923. 10.1038/sj.emboj.7601633.
4. Jäger, S., Handschin, C., St.-Pierre, J., and Spiegelman, B.M. (2007). AMP-activated protein kinase (AMPK) action in skeletal muscle via direct phosphorylation of PGC-1α. Proceedings of the National Academy of Sciences *104*, 12017-12022. 10.1073/pnas.0705070104.
5. Ojuka, E.O., Jones, T.E., Han, D.H., Chen, M., and Holloszy, J.O. (2003). Raising Ca 2+ in L6 myotubes mimics effects of exercise on mitochondrial biogenesis in muscle. The FASEB Journal *17*, 675-681. 10.1096/fj.02-0951com.
6. Cantó, C., Gerhart-Hines, Z., Feige, J.N., Lagouge, M., Noriega, L., Milne, J.C., Elliott, P.J., Puigserver, P., and Auwerx, J. (2009). AMPK regulates energy expenditure by modulating NAD+ metabolism and SIRT1 activity. Nature *458*, 1056-1060. 10.1038/nature07813.
7. Scarpulla, R.C. (2011). Metabolic control of mitochondrial biogenesis through the PGC-1 family regulatory network. Biochimica et Biophysica Acta (BBA) - Molecular Cell Research *1813*, 1269-1278. 10.1016/j.bbamcr.2010.09.019.
8. Schreiber, S.N., Emter, R., Hock, M.B., Knutti, D., Cardenas, J., Podvinec, M., Oakeley, E.J., and Kralli, A. (2004). The estrogen-related receptor α (ERRα) functions in PPARγ coactivator 1α (PGC-1α)-induced mitochondrial biogenesis. Proceedings of the National Academy of Sciences *101*, 6472-6477. 10.1073/pnas.0308686101.
9. Schreiber, S.N., Knutti, D., Brogli, K., Uhlmann, T., and Kralli, A. (2003). The Transcriptional Coactivator PGC-1 Regulates the Expression and Activity of the Orphan Nuclear Receptor Estrogen-Related Receptor α (ERRα). Journal of Biological Chemistry *278*, 9013-9018. 10.1074/jbc.M212923200.
10. Virbasius, J.V., and Scarpulla, R.C. (1994). Activation of the human mitochondrial transcription factor A gene by nuclear respiratory factors: a potential regulatory link between nuclear and mitochondrial gene expression in organelle biogenesis. Proceedings of the National Academy of Sciences *91*, 1309-1313. 10.1073/pnas.91.4.1309.
11. Kleele, T., Rey, T., Winter, J., Zaganelli, S., Mahecic, D., Perreten Lambert, H., Ruberto, F.P., Nemir, M., Wai, T., Pedrazzini, T., and Manley, S. (2021). Distinct fission signatures predict mitochondrial degradation or biogenesis. Nature *593*, 435-439. 10.1038/s41586-021-03510-6.
12. Lewis, S.C., Uchiyama, L.F., and Nunnari, J. (2016). ER-mitochondria contacts couple mtDNA synthesis with mitochondrial division in human cells. Science *353*, aaf5549. 10.1126/science.aaf5549.
13. Cardanho-Ramos, C., and Morais, V.A. (2021). Mitochondrial Biogenesis in Neurons: How and Where. International Journal of Molecular Sciences *22*, 13059. 10.3390/ijms222313059.
14. Davis, A.F., and Clayton, D.A. (1996). In situ localization of mitochondrial DNA replication in intact mammalian cells. Journal of Cell Biology *135*, 883-893. 10.1083/jcb.135.4.883.

15. Schultz, R.A., Swoap, S.J., McDaniel, L.D., Zhang, B., Koon, E.C., Garry, D.J., Li, K., and Williams, R.S. (1998). Differential Expression of Mitochondrial DNA Replication Factors in Mammalian Tissues. Journal of Biological Chemistry *273*, 3447-3451. 10.1074/jbc.273.6.3447.
16. Amiri, M., and Hollenbeck, P.J. (2008). Mitochondrial biogenesis in the axons of vertebrate peripheral neurons. Dev Neurobiol *68*, 1348-1361. 10.1002/dneu.20668.
17. Cioni, J.M., Lin, J.Q., Holtermann, A.V., Koppers, M., Jakobs, M.A.H., Azizi, A., Turner-Bridger, B., Shigeoka, T., Franze, K., Harris, W.A., and Holt, C.E. (2019). Late Endosomes Act as mRNA Translation Platforms and Sustain Mitochondria in Axons. Cell *176*, 56-72 e15. 10.1016/j.cell.2018.11.030.
18. Kuzniewska, B., Cysewski, D., Wasilewski, M., Sakowska, P., Milek, J., Kulinski, T.M., Winiarski, M., Kozielewicz, P., Knapska, E., Dadlez, M., et al. (2020). Mitochondrial protein biogenesis in the synapse is supported by local translation. EMBO Rep *21*, e48882. 10.15252/embr.201948882.
19. Van Laar, V.S., Arnold, B., Howlett, E.H., Calderon, M.J., St Croix, C.M., Greenamyre, J.T., Sanders, L.H., and Berman, S.B. (2018). Evidence for Compartmentalized Axonal Mitochondrial Biogenesis: Mitochondrial DNA Replication Increases in Distal Axons As an Early Response to Parkinson's Disease-Relevant Stress. J Neurosci *38*, 7505-7515. 10.1523/JNEUROSCI.0541-18.2018.
20. Hollenbeck, P.J., and Saxton, W.M. (2005). The axonal transport of mitochondria. J Cell Sci *118*, 5411-5419. 10.1242/jcs.02745.
21. Pilling, A.D., Horiuchi, D., Lively, C.M., and Saxton, W.M. (2006). Kinesin-1 and Dynein are the primary motors for fast transport of mitochondria in Drosophila motor axons. Mol Biol Cell *17*, 2057-2068. 10.1091/mbc.e05-06-0526.
22. Saxton, W.M., and Hollenbeck, P.J. (2012). The axonal transport of mitochondria. J Cell Sci *125*, 2095-2104. 10.1242/jcs.053850.
23. Schnapp, B.J., and Reese, T.S. (1989). Dynein is the motor for retrograde axonal transport of organelles. Proc Natl Acad Sci U S A *86*, 1548-1552. 10.1073/pnas.86.5.1548.
24. Canty, J.T., Hensley, A., Aslan, M., Jack, A., and Yildiz, A. (2023). TRAK adaptors regulate the recruitment and activation of dynein and kinesin in mitochondrial transport. Nat Commun *14*, 1376. 10.1038/s41467-023-36945-8.
25. Glater, E.E., Megeath, L.J., Stowers, R.S., and Schwarz, T.L. (2006). Axonal transport of mitochondria requires milton to recruit kinesin heavy chain and is light chain independent. J Cell Biol *173*, 545-557. 10.1083/jcb.200601067.
26. Stowers, R.S., Megeath, L.J., Gorska-Andrzejak, J., Meinertzhagen, I.A., and Schwarz, T.L. (2002). Axonal transport of mitochondria to synapses depends on milton, a novel Drosophila protein. Neuron *36*, 1063-1077. 10.1016/s0896-6273(02)01094-2.
27. Guo, X., Macleod, G.T., Wellington, A., Hu, F., Panchumarthi, S., Schoenfield, M., Marin, L., Charlton, M.P., Atwood, H.L., and Zinsmaier, K.E. (2005). The GTPase dMiro is required for axonal transport of mitochondria to Drosophila synapses. Neuron *47*, 379-393. 10.1016/j.neuron.2005.06.027.
28. Fenton, A.R., Jongens, T.A., and Holzbaur, E.L.F. (2021). Mitochondrial adaptor TRAK2 activates and functionally links opposing kinesin and dynein motors. Nat Commun *12*, 4578. 10.1038/s41467-021-24862-7.

29. MacAskill, A.F., Brickley, K., Stephenson, F.A., and Kittler, J.T. (2009). GTPase dependent recruitment of Grif-1 by Miro1 regulates mitochondrial trafficking in hippocampal neurons. Mol Cell Neurosci *40*, 301-312. 10.1016/j.mcn.2008.10.016.
30. MacAskill, A.F., and Kittler, J.T. (2010). Control of mitochondrial transport and localization in neurons. Trends Cell Biol *20*, 102-112. 10.1016/j.tcb.2009.11.002.
31. Han, S.M., Baig, H.S., and Hammarlund, M. (2016). Mitochondria Localize to Injured Axons to Support Regeneration. Neuron *92*, 1308-1323. 10.1016/j.neuron.2016.11.025.
32. Zhou, B., Yu, P., Lin, M.Y., Sun, T., Chen, Y., and Sheng, Z.H. (2016). Facilitation of axon regeneration by enhancing mitochondrial transport and rescuing energy deficits. J Cell Biol *214*, 103-119. 10.1083/jcb.201605101.
33. Campbell, P.D., Shen, K., Sapio, M.R., Glenn, T.D., Talbot, W.S., and Marlow, F.L. (2014). Unique function of Kinesin Kif5A in localization of mitochondria in axons. J Neurosci *34*, 14717-14732. 10.1523/JNEUROSCI.2770-14.2014.
34. Drerup, C.M., Herbert, A.L., Monk, K.R., and Nechiporuk, A.V. (2017). Regulation of mitochondria-dynactin interaction and mitochondrial retrograde transport in axons. eLife *6*, e22234. 10.7554/eLife.22234.
35. Joshi, D.C., Zhang, C.L., Babujee, L., Vevea, J.D., August, B.K., Sheng, Z.H., Chapman, E.R., Gomez, T.M., and Chiu, S.Y. (2019). Inappropriate Intrusion of an Axonal Mitochondrial Anchor into Dendrites Causes Neurodegeneration. Cell Rep *29*, 685-696 e685. 10.1016/j.celrep.2019.09.012.
36. Mandal, A., Wong, H.-T.C., Pinter, K., Mosqueda, N., Beirl, A., Lomash, R.M., Won, S., Kindt, K.S., and Drerup, C.M. (2021). Retrograde Mitochondrial Transport Is Essential for Organelle Distribution and Health in Zebrafish Neurons. The Journal of Neuroscience *41*, 1371-1392. 10.1523/JNEUROSCI.1316-20.2020.
37. Metcalfe, W.K., Kimmel, C.B., and Schabtach, E. (1985). Anatomy of the posterior lateral line system in young larvae of the zebrafish. The Journal of Comparative Neurology *233*, 377-389. 10.1002/cne.902330307.
38. Kindt, Katie S., Finch, G., and Nicolson, T. (2012). Kinocilia Mediate Mechanosensitivity in Developing Zebrafish Hair Cells. Developmental Cell *23*, 329-341. 10.1016/j.devcel.2012.05.022.
39. Eckley, D.M., and Schroer, T.A. (2003). Interactions between the evolutionarily conserved, actin-related protein, Arp11, actin, and Arp1. Mol Biol Cell *14*, 2645-2654. 10.1091/mbc.e03-01-0049.
40. Rajala, N., Gerhold, J.M., Martinsson, P., Klymov, A., and Spelbrink, J.N. (2014). Replication factors transiently associate with mtDNA at the mitochondrial inner membrane to facilitate replication. Nucleic Acids Research *42*, 952-967. 10.1093/nar/gkt988.
41. Kaufman, B.A., Durisic, N., Mativetsky, J.M., Costantino, S., Hancock, M.A., Grutter, P., and Shoubridge, E.A. (2007). The Mitochondrial Transcription Factor TFAM Coordinates the Assembly of Multiple DNA Molecules into Nucleoid-like Structures. Molecular Biology of the Cell *18*, 3225-3236. 10.1091/mbc.e07-05-0404.
42. Choi, H.M.T., Schwarzkopf, M., Fornace, M.E., Acharya, A., Artavanis, G., Stegmaier, J., Cunha, A., and Pierce, N.A. (2018). Third-generation in situ hybridization chain reaction: multiplexed, quantitative, sensitive, versatile, robust. Development *145*, dev165753. 10.1242/dev.165753.

43. Kawano, D., Pinter, K., Chlebowski, M., Petralia, R.S., Wang, Y.-X., Nechiporuk, A.V., and Drerup, C.M. (2022). NudC regulated Lis1 stability is essential for the maintenance of dynamic microtubule ends in axon terminals. iScience *25*, 105072. 10.1016/j.isci.2022.105072.
44. Lloyd, Thomas E., Machamer, J., O'Hara, K., Kim, Ji H., Collins, Sarah E., Wong, Man Y., Sahin, B., Imlach, W., Yang, Y., Levitan, Edwin S., et al. (2012). The p150Glued CAP-Gly Domain Regulates Initiation of Retrograde Transport at Synaptic Termini. Neuron *74*, 344-360. 10.1016/j.neuron.2012.02.026.
45. McGrail, M., Gepner, J., Silvanovich, A., Ludmann, S., Serr, M., and Hays, T.S. (1995). Regulation of cytoplasmic dynein function in vivo by the Drosophila Glued complex. The Journal of cell biology *131*, 411-425. 10.1083/jcb.131.2.411.
46. Moughamian, Armen J., and Holzbaur, Erika L.F. (2012). Dynactin Is Required for Transport Initiation from the Distal Axon. Neuron *74*, 331-343. 10.1016/j.neuron.2012.02.025.
47. Rath, S., Sharma, R., Gupta, R., Ast, T., Chan, C., Durham, T.J., Goodman, R.P., Grabarek, Z., Haas, M.E., Hung, W.H.W., et al. (2020). MitoCarta3.0: an updated mitochondrial proteome now with sub-organelle localization and pathway annotations. Nucleic Acids Research *49*, D1541-D1547. 10.1093/nar/gkaa1011.
48. Wong, H.-T.C., Lang, A.E., Stein, C., and Drerup, C.M. (2024). ALS-Linked VapB P56S Mutation Alters Neuronal Mitochondrial Turnover at the Synapse. The Journal of Neuroscience *44*, e0879242024. 10.1523/JNEUROSCI.0879-24.2024.
49. Mandal, A., Pinter, K., and Drerup, C.M. (2018). Analyzing Neuronal Mitochondria in vivo Using Fluorescent Reporters in Zebrafish. Frontiers in Cell and Developmental Biology *6*, 144. 10.3389/fcell.2018.00144.
50. Smirnova, E., Griparic, L., Shurland, D.L., and van der Bliek, A.M. (2001). Dynamin-related protein Drp1 is required for mitochondrial division in mammalian cells. Mol Biol Cell *12*, 2245-2256. 10.1091/mbc.12.8.2245.
51. Zhu, P.P., Patterson, A., Stadler, J., Seeburg, D.P., Sheng, M., and Blackstone, C. (2004). Intra- and intermolecular domain interactions of the C-terminal GTPase effector domain of the multimeric dynamin-like GTPase Drp1. J Biol Chem *279*, 35967-35974. 10.1074/jbc.M404105200.
52. Renken, C.J., Kim, S., Wu, Y., Hammarlund, M., and Yogev, S. (2024). Cytoplasmic ribosomes hitchhike on mitochondria to dendrites. 10.1101/2024.09.13.612863.
53. Horie, C., Suzuki, H., Sakaguchi, M., and Mihara, K. (2002). Characterization of Signal That Directs C-Tail–anchored Proteins to Mammalian Mitochondrial Outer Membrane. Molecular Biology of the Cell *13*, 1615-1625. 10.1091/mbc.01-12-0570.
54. Yang, R., Bentley, M., Huang, C.-F., and Banker, G. (2016). Analyzing kinesin motor domain translocation in cultured hippocampal neurons. In Methods in Cell Biology, (Elsevier), pp. 217-232.
55. Eichner, L.J., and Giguère, V. (2011). Estrogen related receptors (ERRs): A new dawn in transcriptional control of mitochondrial gene networks. Mitochondrion *11*, 544-552. 10.1016/j.mito.2011.03.121.
56. Hock, M.B., and Kralli, A. (2009). Transcriptional Control of Mitochondrial Biogenesis and Function. Annual Review of Physiology *71*, 177-203. 10.1146/annurev.physiol.010908.163119.

57. Fan, W., He, N., Lin, C.S., Wei, Z., Hah, N., Waizenegger, W., He, M.-X., Liddle, C., Yu, R.T., Atkins, A.R., et al. (2018). ERRγ Promotes Angiogenesis, Mitochondrial Biogenesis, and Oxidative Remodeling in PGC1α/β-Deficient Muscle. Cell Reports *22*, 2521-2529. 10.1016/j.celrep.2018.02.047.
58. Huss, J.M., Torra, I.P., Staels, B., Giguère, V., and Kelly, D.P. (2004). Estrogen-Related Receptor α Directs Peroxisome Proliferator-Activated Receptor α Signaling in the Transcriptional Control of Energy Metabolism in Cardiac and Skeletal Muscle. Molecular and Cellular Biology *24*, 9079-9091. 10.1128/MCB.24.20.9079-9091.2004.
59. Pei, L., Mu, Y., Leblanc, M., Alaynick, W., Barish, Grant D., Pankratz, M., Tseng, Tiffany W., Kaufman, S., Liddle, C., Yu, Ruth T., et al. (2015). Dependence of Hippocampal Function on ERRγ-Regulated Mitochondrial Metabolism. Cell Metabolism *21*, 628-636. 10.1016/j.cmet.2015.03.004.
60. Howitz, K.T., Bitterman, K.J., Cohen, H.Y., Lamming, D.W., Lavu, S., Wood, J.G., Zipkin, R.E., Chung, P., Kisielewski, A., Zhang, L.-L., et al. (2003). Small molecule activators of sirtuins extend Saccharomyces cerevisiae lifespan. Nature *425*, 191-196. 10.1038/nature01960.
61. Lopes Costa, A., Le Bachelier, C., Mathieu, L., Rotig, A., Boneh, A., De Lonlay, P., Tarnopolsky, M.A., Thorburn, D.R., Bastin, J., and Djouadi, F. (2014). Beneficial effects of resveratrol on respiratory chain defects in patients' fibroblasts involve estrogen receptor and estrogen-related receptor alpha signaling. Human Molecular Genetics *23*, 2106-2119. 10.1093/hmg/ddt603.
62. Sopariwala, D.H., Rios, A.S., Park, M.K., Song, M.S., Kumar, A., and Narkar, V.A. (2022). Estrogen-related receptor alpha is an AMPK -regulated factor that promotes ischemic muscle revascularization and recovery in diet-induced obese mice. FASEB BioAdvances *4*, 602-618. 10.1096/fba.2022-00015.
63. Wilson, B.J., Tremblay, A.M., Deblois, G., Sylvain-Drolet, G., and Giguère, V. (2010). An Acetylation Switch Modulates the Transcriptional Activity of Estrogen-Related Receptor α. Molecular Endocrinology *24*, 1349-1358. 10.1210/me.2009-0441.
64. Yan, M., Audet-Walsh, É., Manteghi, S., Dufour, C.R., Walker, B., Baba, M., St-Pierre, J., Giguère, V., and Pause, A. (2016). Chronic AMPK activation via loss of FLCN induces functional beige adipose tissue through PGC-1α/ERRα. Genes & Development *30*, 1034-1046. 10.1101/gad.281410.116.
65. Corton, J.M., Gillespie, J.G., Hawley, S.A., and Hardie, D.G. (1995). 5-Aminoimidazole-4-Carboxamide Ribonucleoside. A Specific Method for Activating AMP-Activated Protein Kinase in Intact Cells? European Journal of Biochemistry *229*, 558-565. 10.1111/j.1432-1033.1995.tb20498.x.
66. Mosser, E.A., Chiu, C.N., Tamai, T.K., Hirota, T., Li, S., Hui, M., Wang, A., Singh, C., Giovanni, A., Kay, S.A., and Prober, D.A. (2019). Identification of pathways that regulate circadian rhythms using a larval zebrafish small molecule screen. Scientific Reports *9*, 12405. 10.1038/s41598-019-48914-7.
67. Alano, C.C., Tran, A., Tao, R., Ying, W., Karliner, J.S., and Swanson, R.A. (2007). Differences among cell types in NAD(+) compartmentalization: a comparison of neurons, astrocytes, and cardiac myocytes. J Neurosci Res *85*, 3378-3385. 10.1002/jnr.21479.
68. Hu, Q., Wu, D., Walker, M., Wang, P., Tian, R., and Wang, W. (2021). Genetically encoded biosensors for evaluating NAD(+)/NADH ratio in cytosolic and mitochondrial compartments. Cell Rep Methods *1*. 10.1016/j.crmeth.2021.100116.

69. Wareski, P., Vaarmann, A., Choubey, V., Safiulina, D., Liiv, J., Kuum, M., and Kaasik, A. (2009). PGC-1α and PGC-1B Regulate Mitochondrial Density in Neurons. Journal of Biological Chemistry *284*, 21379-21385. 10.1074/jbc.M109.018911.
70. Cambronne, X.A., Stewart, M.L., Kim, D., Jones-Brunette, A.M., Morgan, R.K., Farrens, D.L., Cohen, M.S., and Goodman, R.H. (2016). Biosensor reveals multiple sources for mitochondrial NAD(+). Science *352*, 1474-1477. 10.1126/science.aad5168.
71. Chen, Y., Jiang, Y., Yang, Y., Huang, X., and Sun, C. (2021). SIRT1 Protects Dopaminergic Neurons in Parkinson's Disease Models via PGC-1α-Mediated Mitochondrial Biogenesis. Neurotoxicity Research *39*, 1393-1404. 10.1007/s12640-021-00392-4.
72. Hatsuda, A., Kurisu, J., Fujishima, K., Kawaguchi, A., Ohno, N., and Kengaku, M. (2023). Calcium signals tune AMPK activity and mitochondrial homeostasis in dendrites of developing neurons. Development *150*, dev201930. 10.1242/dev.201930.
73. Eudy, J.D., Yao, S., Weston, M.D., Ma-Edmonds, M., Talmadge, C.B., Cheng, J.J., Kimberling, W.J., and Sumegi, J. (1998). Isolation of a Gene Encoding a Novel Member of the Nuclear Receptor Superfamily from the Critical Region of Usher Syndrome Type IIa at 1q41. Genomics *50*, 382-384. 10.1006/geno.1998.5345.
74. Giguère, V., Yang, N., Segui, P., and Evans, R.M. (1988). Identification of a new class of steroid hormone receptors. Nature *331*, 91-94. 10.1038/331091a0.
75. Johnston, S.D., Liu, X., Zuo, F., Eisenbraun, T.L., Wiley, S.R., Kraus, R.J., and Mertz, J.E. (1997). Estrogen-Related Receptor α1 Functionally Binds as a Monomer to Extended Half-Site Sequences Including Ones Contained within Estrogen-Response Elements. Molecular Endocrinology *11*, 342-352. 10.1210/mend.11.3.9897.
76. Huss, J.M., Garbacz, W.G., and Xie, W. (2015). Constitutive activities of estrogen-related receptors: Transcriptional regulation of metabolism by the ERR pathways in health and disease. Biochimica et Biophysica Acta (BBA) - Molecular Basis of Disease *1852*, 1912-1927. 10.1016/j.bbadis.2015.06.016.
77. McMeekin, L.J., Joyce, K.L., Jenkins, L.M., Bohannon, B.M., Patel, K.D., Bohannon, A.S., Patel, A., Fox, S.N., Simmons, M.S., Day, J.J., et al. (2021). Estrogen-related Receptor Alpha (ERRα) is Required for PGC-1α-dependent Gene Expression in the Mouse Brain. Neuroscience *479*, 70-90. 10.1016/j.neuroscience.2021.10.007.
78. Lydon, J.P., Power, R.F., and Conneely, O.M. (1992). Differential modes of activation define orphan subclasses within the steroid/thyroid receptor superfamily. Gene Expr *2*, 273-283.
79. Vernier, M., and Giguère, V. (2021). Aging, senescence and mitochondria: the PGC-1/ERR axis. Journal of Molecular Endocrinology *66*, R1-R14. 10.1530/JME-20-0196.
80. Yu, L., and Yang, S.J. (2010). AMP-activated protein kinase mediates activity-dependent regulation of peroxisome proliferator-activated receptor γ coactivator-1α and nuclear respiratory factor 1 expression in rat visual cortical neurons. Neuroscience *169*, 23-38. 10.1016/j.neuroscience.2010.04.063.
81. Lagouge, M., Argmann, C., Gerhart-Hines, Z., Meziane, H., Lerin, C., Daussin, F., Messadeq, N., Milne, J., Lambert, P., Elliott, P., et al. (2006). Resveratrol Improves Mitochondrial Function and Protects against Metabolic Disease by Activating SIRT1 and PGC-1α. Cell *127*, 1109-1122. 10.1016/j.cell.2006.11.013.
82. Blander, G., and Guarente, L. (2004). The Sir2 family of protein deacetylases. Annu Rev Biochem *73*, 417-435. 10.1146/annurev.biochem.73.011303.073651.

83. Michishita, E., Park, J.Y., Burneskis, J.M., Barrett, J.C., and Horikawa, I. (2005). Evolutionarily conserved and nonconserved cellular localizations and functions of human SIRT proteins. Mol Biol Cell *16*, 4623-4635. 10.1091/mbc.e05-01-0033.
84. Qin, W., Haroutunian, V., Katsel, P., Cardozo, C.P., Ho, L., Buxbaum, J.D., and Pasinetti, G.M. (2009). PGC-1α Expression Decreases in the Alzheimer Disease Brain as a Function of Dementia. Archives of Neurology *66*. 10.1001/archneurol.2008.588.
85. Sheng, B., Wang, X., Su, B., Lee, H.-g., Casadesus, G., Perry, G., and Zhu, X. (2012). Impaired mitochondrial biogenesis contributes to mitochondrial dysfunction in Alzheimer's disease: Impaired mitochondrial biogenesis in AD. Journal of Neurochemistry *120*, 419-429. 10.1111/j.1471-4159.2011.07581.x.
86. Shin, J.-H., Ko, Han S., Kang, H., Lee, Y., Lee, Y.-I., Pletinkova, O., Troconso, Juan C., Dawson, Valina L., and Dawson, Ted M. (2011). PARIS (ZNF746) Repression of PGC-1α Contributes to Neurodegeneration in Parkinson's Disease. Cell *144*, 689-702. 10.1016/j.cell.2011.02.010.
87. Stevens, D.A., Lee, Y., Kang, H.C., Lee, B.D., Lee, Y.-I., Bower, A., Jiang, H., Kang, S.-U., Andrabi, S.A., Dawson, V.L., et al. (2015). Parkin loss leads to PARIS-dependent declines in mitochondrial mass and respiration. Proceedings of the National Academy of Sciences *112*, 11696-11701. 10.1073/pnas.1500624112.
88. Westerfield, M. (1993). The zebrafish book: a guide for the laboratory use of zebrafish (Brachydanio rerio).
89. Kimmel, C.B., Ballard, W.W., Kimmel, S.R., Ullmann, B., and Schilling, T.F. (1995). Stages of embryonic development of the zebrafish. Developmental Dynamics *203*, 253-310. 10.1002/aja.1002030302.
90. Kwan, K.M., Fujimoto, E., Grabher, C., Mangum, B.D., Hardy, M.E., Campbell, D.S., Parant, J.M., Yost, H.J., Kanki, J.P., and Chien, C.B. (2007). The Tol2kit: A multisite gateway-based construction kit for Tol2 transposon transgenesis constructs. Developmental Dynamics *236*, 3088-3099. 10.1002/dvdy.21343.
91. Gibson, D.G., Young, L., Chuang, R.-Y., Venter, J.C., Hutchison, C.A., and Smith, H.O. (2009). Enzymatic assembly of DNA molecules up to several hundred kilobases. Nature Methods *6*, 343-345. 10.1038/nmeth.1318.
92. Huang, C.f., and Banker, G. (2012). The Translocation Selectivity of the Kinesins that Mediate Neuronal Organelle Transport. Traffic *13*, 549-564. 10.1111/j.1600-0854.2011.01325.x.
93. Zhang, Q., Li, S., Wong, H.C., He, X.J., Beirl, A., Petralia, R.S., Wang, Y.X., and Kindt, K.S. (2018). Synaptically silent sensory hair cells in zebrafish are recruited after damage. Nat Commun *9*, 1388. 10.1038/s41467-018-03806-8.
94. Mo, W., and Nicolson, T. (2011). Both Pre- and Postsynaptic Activity of Nsf Prevents Degeneration of Hair-Cell Synapses. PLoS ONE *6*, e27146. 10.1371/journal.pone.0027146.
95. Drerup, C.M., and Nechiporuk, A.V. (2013). JNK-Interacting Protein 3 Mediates the Retrograde Transport of Activated c-Jun N-Terminal Kinase and Lysosomes. PLoS Genetics *9*, e1003303. 10.1371/journal.pgen.1003303.
96. Drerup, C.M., and Nechiporuk, A.V. (2016). In vivo analysis of axonal transport in zebrafish. Methods in cell biology *131*, 311-329. 10.1016/bs.mcb.2015.06.007.

97. Preibisch, S., Saalfeld, S., and Tomancak, P. (2009). Globally optimal stitching of tiled 3D microscopic image acquisitions. Bioinformatics *25*, 1463-1465. 10.1093/bioinformatics/btp184.
98. Schindelin, J., Arganda-Carreras, I., Frise, E., Kaynig, V., Longair, M., Pietzsch, T., Preibisch, S., Rueden, C., Saalfeld, S., Schmid, B., et al. (2012). Fiji: an open-source platform for biological-image analysis. Nature Methods *9*, 676-682. 10.1038/nmeth.2019.
99. Thisse, C., and Thisse, B. (2008). High-resolution in situ hybridization to whole-mount zebrafish embryos. Nature Protocols *3*, 59-69. 10.1038/nprot.2007.514.
100. Logel, J., Dill, D., and Leonard, S. (1992). Synthesis of cRNA probes from PCR-generated DNA. BioTechniques *13*, 604-610.
101. Bolger, A.M., Lohse, M., and Usadel, B. (2014). Trimmomatic: a flexible trimmer for Illumina sequence data. Bioinformatics *30*, 2114-2120. 10.1093/bioinformatics/btu170.
102. Dobin, A., Davis, C.A., Schlesinger, F., Drenkow, J., Zaleski, C., Jha, S., Batut, P., Chaisson, M., and Gingeras, T.R. (2013). STAR: ultrafast universal RNA-seq aligner. Bioinformatics *29*, 15-21. 10.1093/bioinformatics/bts635.
103. Liao, Y., Smyth, G.K., and Shi, W. (2014). featureCounts: an efficient general purpose program for assigning sequence reads to genomic features. Bioinformatics *30*, 923-930. 10.1093/bioinformatics/btt656.
104. Love, M.I., Huber, W., and Anders, S. (2014). Moderated estimation of fold change and dispersion for RNA-seq data with DESeq2. Genome Biology *15*, 550. 10.1186/s13059-014-0550-8.
105. Yu, G. (2024). Thirteen years of clusterProfiler. The Innovation *5*, 100722. 10.1016/j.xinn.2024.100722.
106. Kolberg, L., Raudvere, U., Kuzmin, I., Adler, P., Vilo, J., and Peterson, H. (2023). g:Profiler—interoperable web service for functional enrichment analysis and gene identifier mapping (2023 update). Nucleic Acids Research *51*, W207-W212. 10.1093/nar/gkad347.
107. Puente-Santamaria, L., Wasserman, W.W., and Del Peso, L. (2019). TFEA.ChIP: a tool kit for transcription factor binding site enrichment analysis capitalizing on ChIP-seq datasets. Bioinformatics *35*, 5339-5340. 10.1093/bioinformatics/btz573.
108. Elizarraras, J.M., Liao, Y., Shi, Z., Zhu, Q., Pico, Alexander R., and Zhang, B. (2024). WebGestalt 2024: faster gene set analysis and new support for metabolomics and multi-omics. Nucleic Acids Research *52*, W415-W421. 10.1093/nar/gkae456.
109. Wickham, H. (2016). ggplot2: Elegant Graphics for Data Analysis, 2nd 2016 Edition (Springer International Publishing : Imprint: Springer).
110. Lister, J.A., Robertson, C.P., Lepage, T., Johnson, S.L., and Raible, D.W. (1999). nacre encodes a zebrafish microphthalmia-related protein that regulates neural-crest-derived pigment cell fate. Development *126*, 3757-3767. 10.1242/dev.126.17.3757.
111. Obholzer, N., Wolfson, S., Trapani, J.G., Mo, W., Nechiporuk, A., Busch-Nentwich, E., Seiler, C., Sidi, S., Söllner, C., Duncan, R.N., et al. (2008). Vesicular Glutamate Transporter 3 Is Required for Synaptic Transmission in Zebrafish Hair Cells. The Journal of Neuroscience *28*, 2110-2118. 10.1523/JNEUROSCI.5230-07.2008.